

Electronic dynamics created at conical intersections and its dephasing in aqueous solution

Yi-Ping Chang^{1,2†}, Tadas Balciunas^{1,3†}, Zhong Yin^{3,4*†}, Marin Sapunar^{5†}, Bruno N. C. Tenorio^{6,7†}, Alexander C. Paul^{8†}, Shota Tsuru^{9,10}, Henrik Koch^{8*}, Jean–Pierre Wolf^{1*}, Sonia Coriani^{6*} and Hans Jakob Wörner^{3*}

¹GAP–Biophotonics, Université de Genève, 1205 Geneva, Switzerland.

²European XFEL, 22689 Schenefeld, Germany.

³Laboratory of Physical Chemistry, ETH Zürich, 8093 Zürich, Switzerland.

⁴International Center for Synchrotron Radiation Innovation Smart, Tohoku University, 980-8577 Sendai, Japan.

⁵Division of Physical Chemistry, Ruđer Bošković Institute, 10000 Zagreb, Croatia.

⁶Department of Chemistry, Technical University of Denmark, 2800 Kongens Lyngby, Denmark.

⁷Instituto Madrileño de Estudios Avanzados en Nanociencia, IMDEA-Nanociencia, 28049 Madrid, Spain.

⁸Department of Chemistry, Norwegian University of Science and Technology, 7034 Trondheim, Norway.

⁹Lehrstuhl für Theoretische Chemie, Ruhr-Universität Bochum, 44801 Bochum, Germany.

¹⁰RIKEN Center for Computational Science, RIKEN, 650-0047 Kobe, Japan.

*Corresponding author(s). E-mail(s): yinz@tohoku.ac.jp; henrik.koch@ntnu.no; jean-pierre.wolf@unige.ch; soco@kemi.dtu.dk; hwoerner@ethz.ch;

†These authors contributed equally to this work.

Abstract

A dynamical rearrangement in the electronic structure of a molecule can be driven by different phenomena, including nuclear motion, electronic coherence or electron correlation. Recording such electronic dynamics and identifying their fate in aqueous solution has remained a challenge. Here, we reveal the electronic dynamics induced by electronic relaxation through conical intersections in pyrazine molecules using X-ray spectroscopy. We show that the ensuing created dynamics corresponds to a cyclic rearrangement of the electronic structure around the aromatic ring. Furthermore, we find that such electronic dynamics are entirely suppressed when pyrazine is dissolved in water. Our observations confirm that conical intersections can create electronic dynamics that are not directly excited by the pump pulse and that aqueous solvation can dephase them in less than 40 fs. These results have implications for the investigation of electronic dynamics created during light-induced molecular dynamics and shed light on their susceptibility to aqueous solvation.

Keywords: Electronic dynamics, X-ray absorption, Water window, Time-resolved XAS, Liquid flat jets

Electronic dynamics are the central concept underlying multiple emerging research fields that range from attosecond spectroscopy [1, 2] over attochemistry [3–6] to quantum biology [7, 8]. Despite their importance, identifying electronic dynamics and distinguishing them from purely vibrational dynamics has remained a major challenge causing numerous controversies. Especially in the case of excited-state dynamics, the distinction of electronic from purely vibrational dynamics often remains out of reach because of the strong coupling between the two types of dynamics in the vicinity of conical intersection (CIs) and/or an insufficient contrast in the sensitivity of the probe to electronic vs. vibrational dynamics. Additionally, an important question for the viability and broader impact of the above-mentioned research areas is the lifetime of electronic dynamics under ambient conditions, which imply a rapidly fluctuating environment [9]. Moreover, many technologically and fundamentally important processes, especially in chemistry and biology, take place in water such that exploiting electronic dynamics in such processes [10] necessitates a method that can trace and disambiguate them in aqueous solutions. Although two-dimensional spectroscopies in the optical domain have in principle such capabilities, the assignment and interpretation of the observed signals often remain sufficiently ambiguous that it has created controversies, e.g., regarding the nature and lifetime of electronic vs. vibrational dynamics observed in light-harvesting systems [7, 8].

Here, we report two experimental breakthroughs, namely (i) the observation of electronic and vibrational dynamics corresponding to a circular rearrangement of the electronic structure that is created by CI dynamics and (ii) their sub-40-fs dephasing induced by aqueous solvation. This has been achieved by directly comparing the dynamics of UV-excited pyrazine in the gas phase and in aqueous solution with a new experimental scheme that unites element specificity, site selectivity, and the transparency of water with the required time resolution. This scheme combines for

the first time one-photon excitation in the ultraviolet (UV) domain with a soft-X-ray probe [11–14] covering the entire water window [15].

The interpretation of our results is supported by the latest advances in quantum-chemical calculations of X-ray absorption (XA) spectra, coupled to nonadiabatic dynamical simulations, which also include solvation effects. These calculations enable an unambiguous assignment of the transient spectral features observed in the experimental spectra.

The heteroaromatic pyrazine molecule ($C_4H_4N_2$), a paradigmatic system for both theoretical and experimental studies of electronically nonadiabatic dynamics, serves as a demonstration of the opportunities opened by our work. The gas-phase measurements indeed show that the electronic relaxation of the initially photoexcited ${}^1B_{2u}(\pi\pi^*)$ state (historically referred to as S_2) through CIs induces electronic and vibrational dynamics involving the ${}^1B_{3u}(n\pi^*)$, known as S_1) and the ${}^1A_u(n\pi^*)$ state.

Our gas-phase results moreover resolve a decades-old controversy between ever-evolving dynamics simulations [16–18] that eventually converged on the prediction of oscillatory population flow [19–24] and experiments that have always negated them. Specifically, time-resolved photoelectron spectroscopy neither revealed the population of the 1A_u state, nor quasi-periodic electronic dynamics [25–29], whereas carbon K-edge transient absorption suggested a population of the 1A_u state in ~ 200 fs, up to ten times slower than the theoretical predictions, and did not reveal any oscillations [13]. As shown in the present work, the key to resolving this controversy was the present experimental advance that combined single-photon excitation with transient absorption spectroscopy at the nitrogen K-edge located at ~ 405 eV. The unprecedented capability of nitrogen K-edge spectroscopy allowed us to not only confirm the predicted oscillatory population flow, but to show that it corresponds to a cyclic rearrangement of the electronic structure around the aromatic ring of pyrazine.

Beyond confirming the possibility of creating electronic dynamics at CIs and resolving the important controversy regarding the electronic-relaxation pathway of the isolated pyrazine molecule, our work additionally reveals the effect of aqueous solvation on the paradigmatic dynamics of this molecule. Specifically, we find that the electronic and vibrational dynamics are completely dephased by solvation within 40 fs. Comparison with dynamical calculations indeed confirms the fact that solvation strongly damps the observed dynamics, but reveals that two explicit water molecules combined with a continuum-solvation model are insufficient to fully capture the dephasing observed in the solution-phase experiments.

Figure 1 provides an overview of the experimental setup (A), the diagram of the relevant orbitals of pyrazine (B) and the XA spectra (C-H). The experiments were performed by photoexciting pyrazine with a 30-fs pump pulse centered at 266 nm, focused to an intensity of $\sim 1 \times 10^{11}$ W/cm² and probing with a soft-X-ray supercontinuum extending beyond 450 eV obtained from high-harmonic generation of a ~ 12 -fs pulse centered at 1.8 μ m in helium. Here, we demonstrate the unique capability of soft-X-ray spectroscopy in the water window to directly compare the dynamics of the same molecules in the gas and solution phase. For this purpose, a dedicated target system has been constructed that allows rapid switching between a gas cell

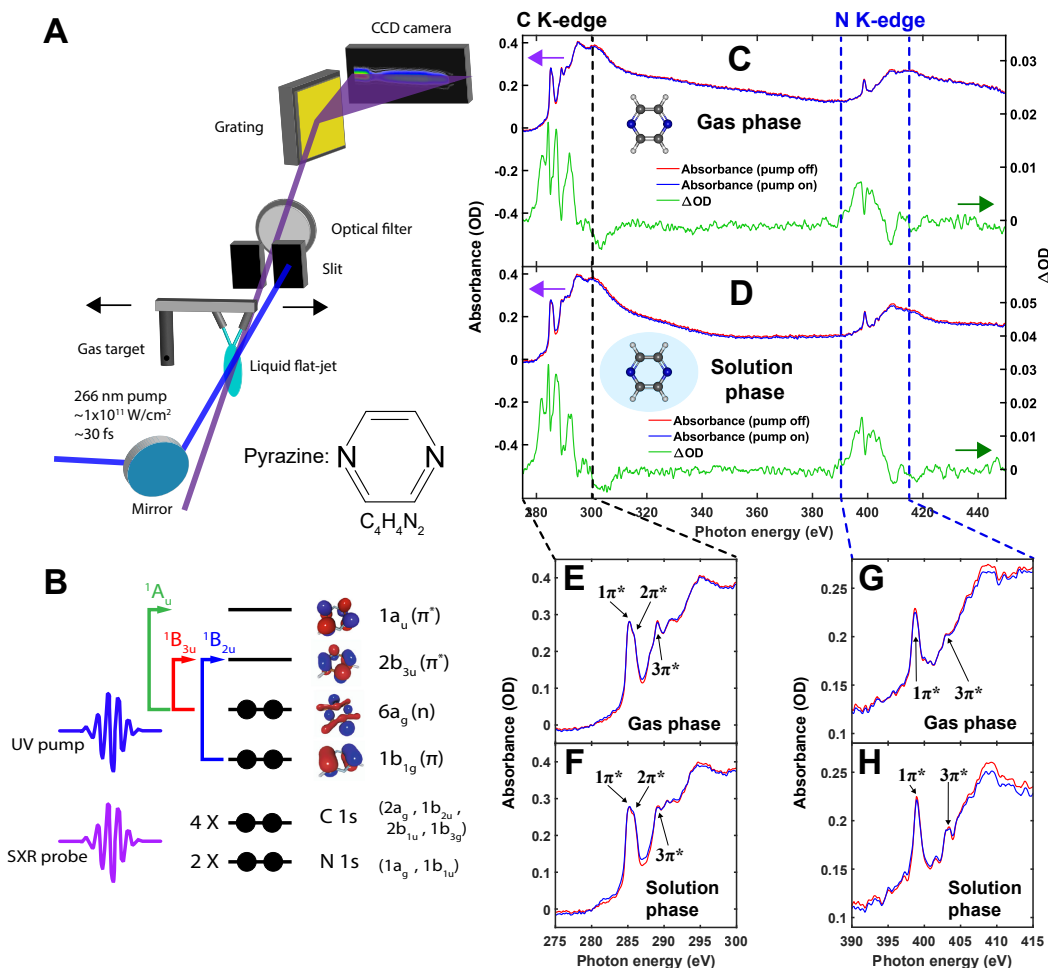


Fig. 1 Overview of the experimental methods and results. (A) Scheme of the experimental setup with both gas and solution flat-jet targets. (B) Molecular-orbital diagram of photoexcitation of pyrazine, with arrows indicating the main transition character of the valence excited states: $^1B_{2u}(\pi\pi^*)$, $^1B_{3u}(n\pi^*)$ and $^1A_u(n\pi^*)$. XA spectra and time-averaged differential absorbances (over 150 fs) covering the water window from carbon to nitrogen K-edges for: (C) the gas phase and (D) the solution phase. No energy shift in the ground-state pyrazine (static measurement) at the carbon pre-edge peak (285.3 eV and 285.8 eV) has been observed between the solution/gas phase. The nitrogen pre-edge peak has a value of 398.7 eV in the gas phase compared to 398.9 eV in solution phase, with an energy shift of about 0.2 eV. (E,F) Zoomed-in on the carbon K-edge. (G,H) Zoomed-in on the nitrogen K-edge.

delivering an effusive beam of pyrazine vapor and a liquid flat jet running a 5M aqueous solution of pyrazine. More details on the experimental setup are given in the supporting information (SI).

Figure 1C, D shows the static XA spectra of gaseous pyrazine and a 5M aqueous pyrazine solution from the carbon to the nitrogen K-edges (red curves), respectively. The time-averaged transient absorption of the excited sample is shown by the blue curves. The differential absorbance spectrum (ΔOD) is shown in green. Magnified portions of the absorption spectra at each edge for both phases are shown in Fig. 1E-H.

At the carbon K-edge, a strong pre-edge absorption feature consisting of two sub-peaks is observed. In both gaseous and aqueous samples, the two pre-edge peaks are at 285.3 eV and 285.8 eV, and can be assigned to $C\ 1s \rightarrow 1\pi^*$ [$2a_g \rightarrow 2b_{3u}$] and $1s \rightarrow 2\pi^*$ [$1b_{3g} \rightarrow 1a_u$] transitions, see SI, Figs. S11, S14. The two final core-excited states have B_{3u} symmetry. In the gas phase, a shoulder at ~ 288.2 eV and a peak at ~ 289.1 eV can be observed, corresponding to $1s \rightarrow \sigma^*/\text{Rydberg}$ and $1s \rightarrow 3\pi^*$ [$2b_{1u} \rightarrow 2b_{2g}$] transitions, respectively. In solution phase, the shoulder at 288.2 eV cannot be resolved, while the peak at ~ 289.0 eV is still present with a small energy shift, but the same assignments as in the gas phase apply.

At the nitrogen K-edge, a single strong pre-edge absorption peak can be observed at 398.7 eV and 398.9 eV, for gaseous and aqueous samples, respectively. This corresponds to the $N\ 1s \rightarrow 1\pi^*$ [$1a_g \rightarrow 2b_{3u}$] transition and indicates an energy shift of +0.2 eV from the gas to the solution phase. In the gas phase, a peak at 402.9 eV corresponding to the $N\ 1s \rightarrow 3\pi^*$ [$1b_{1u} \rightarrow 2b_{2g}$] transition can be observed. In solution phase, a broad peak is seen at ~ 403.3 eV.

The experimental spectra have been calibrated by aligning the experimental gaseous pyrazine carbon and nitrogen pre-edge peaks with synchrotron measurements [30]. In both gas and solution phases, the ΔOD spectra exhibit an increased absorption up to 10 eV below and above the pre-edge. Most of the pre-edge absorption features originate from allowed transitions into valence vacancies created by the pump pulse. The rest of the pre-edge absorption features, as well as the above-pre-edge ones, share core-excitation characters with those of transitions from the ground state.

Figure 2 shows the time-resolved ΔOD spectra of gaseous pyrazine (C&D) and 5M aqueous pyrazine solution (G&H), recorded over a ~ 150 fs time window, with 10 fs steps.

At the carbon K-edge in the gas phase (Fig. 2C), a positive absorption band at 281.4 eV is observed in the first ~ 50 fs, after which it disappears and is replaced by another positive band centered at 282.2 eV, which is broad in the initial ~ 50 -100 fs and then narrows. Concurrently, another positive band at 284.2 eV emerges, with a longer rise time than the previous two bands. At the pre-edge, there is a weak band at ~ 285.7 eV. Above the pre-edge, a positive band at 287.2 eV can be observed rising earlier than the 284.2 eV band. Comparing the 284.2 eV and 287.2 eV bands, reveals that they weakly oscillate out of phase (Fig. S1).

At the carbon K-edge in water solution (Fig. 2G), a broad positive absorption band centered at ~ 281.2 eV is also observed in the first ~ 50 fs, after which it disappears. At the same time, another broad positive band centered at ~ 282 eV is also emerging, such that the band shift from ~ 281.2 to 282 eV is less clear compared to the gas-phase signal. Concurrently, another positive band at 284.4 eV emerges and peaks in intensity at ~ 100 fs before gradually declining. At the pre-edge, there is a weak band at ~ 285.6 eV. Above the pre-edge, a positive band at 286.8 eV can be observed to rise at nearly the same time as the 284.4 eV band, before peaking at ~ 60 fs and subsequently declining in intensity. Comparing the 284.4 eV and 286.8 eV bands, no quantum beats can be identified in either of them.

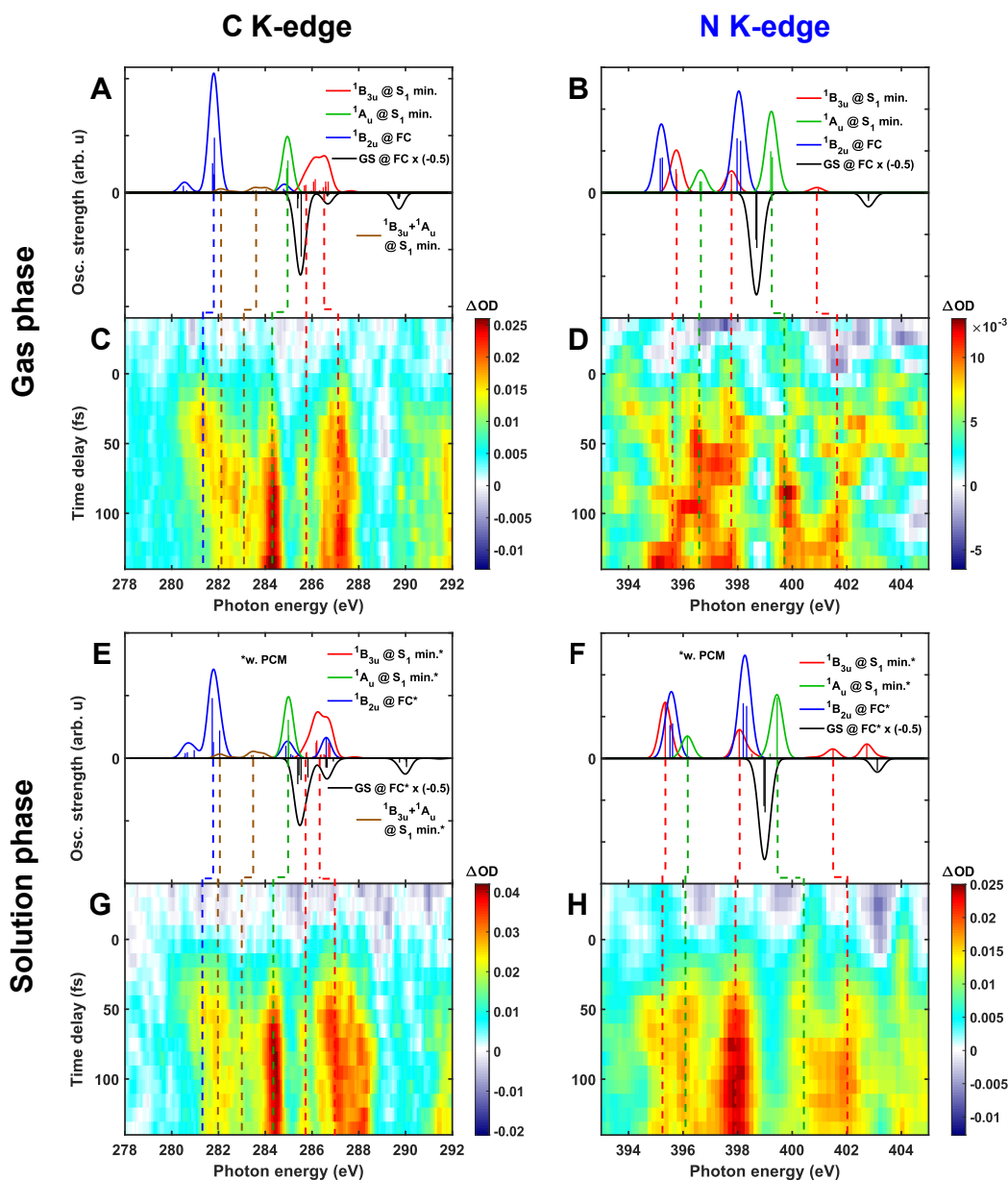


Fig. 2 Time-resolved differential absorbance spectra of pyrazine in the gas and aqueous-solution phases. (C,D) Time-resolved differential absorbance spectra at the carbon and nitrogen K-edges of gaseous pyrazine, respectively. (G,H) Time-resolved differential absorbance spectra at the carbon and nitrogen K-edges of 5M aqueous pyrazine, respectively. (A,E) Carbon K-edge excited-state XA spectra calculated at the RASPT2/RAS2(10e,8o) level at both the Franck-Condon and the relaxed geometry for the first valence excited state (S_1), with and without PCM, respectively. (B,F) same as (A,E) at the nitrogen K-edge.

To assign the bands, both the carbon and nitrogen K-edge excited-state XA spectra were calculated at the RASPT2/RAS2(10e,8o) level at both the Franck-Condon (FC) geometry and the minimum of the first valence-excited singlet state (S_1), the latter obtained with and without polarizable continuum model (PCM) for gaseous and aqueous pyrazine, respectively. The relaxed geometries were obtained at the CASPT2 level. All RAS/CAS calculations were performed using OpenMOLCAS [31]. Additionally, coupled cluster calculations including perturbative triples (CC3) [32, 33]

have been performed. The carbon and nitrogen K-edge excited state XA spectra were calculated at the CC3 level of theory for the gas-phase FC and the S_1 minimum geometry using the eT program [34, 35]. The spectra and more details about the calculations can be found in the SI. Note that, in the gas phase, the potential-energy minimum of the S_1 state has a mixed configuration character, with contributions from both of the $n\pi^*$ states. This is reflected in the simulated spectrum which shows peaks corresponding to the ones seen in both the ${}^1B_{3u}$ and 1A_u states at the FC geometry.

At the carbon K-edge in the gas phase, based on the calculated spectra from Fig. 2A and the schematics in Fig. S9, we can assign the ~ 281.4 eV experimental band to the 281.7 eV $C\ 1s \rightarrow \pi$ from the ${}^1B_{2u}(\pi\pi^*)$ state at the FC geometry, the ~ 282.2 eV band to the 282.1 eV $C\ 1s \rightarrow n$ transitions from both the ${}^1B_{3u}(n\pi^*)$ and ${}^1A_u(n\pi^*)$ states at the S_1 minimum geometry (highly overlapping in this region, see Figure S12), the broad band around 283 eV also to calculated $C\ 1s \rightarrow n$ transitions at around 283.8 eV from both ${}^1B_{3u}(n\pi^*)$ and ${}^1A_u(n\pi^*)$, the 284.2 eV band to the 284.2 eV $C\ 1s \rightarrow \pi^*$ transition from the ${}^1A_u(n\pi^*)$ state at the S_1 minimum geometry, the ~ 285.7 eV band to the 285.9 eV $C\ 1s \rightarrow \pi^*$ transition from the ${}^1B_{3u}(n\pi^*)$ state at the S_1 minimum geometry, and the ~ 287.2 eV band to the 287.2 eV $C\ 1s \rightarrow \pi^*$ transition from the ${}^1B_{3u}(n\pi^*)$ state at the S_1 minimum geometry.

At the carbon K-edge in solution phase, based on the calculated spectra from Fig. 2E, we can assign the ~ 281.2 eV band to the 281.8 eV $C\ 1s \rightarrow \pi$ transition from the ${}^1B_{2u}(\pi\pi^*)$ state at the FC geometry, the ~ 281.9 eV band to the 281.9 eV $C\ 1s \rightarrow n$ transition from both the ${}^1B_{3u}(n\pi^*)$ and ${}^1A_u(n\pi^*)$ states at the S_1 minimum geometry (see Figure S13), the weak broad band around 283 eV to calculated $1s \rightarrow n$ transitions at around 283.6 eV from both ${}^1B_{3u}(n\pi^*)$ and ${}^1A_u(n\pi^*)$, the ~ 284.4 eV band mainly to the 284.7 eV $C\ 1s \rightarrow \pi^*$ transition from the ${}^1A_u(n\pi^*)$ at the S_1 minimum geometry, the ~ 285.6 eV band to the 285.7 eV $C\ 1s \rightarrow \pi^*$ transition from the ${}^1B_{3u}(n\pi^*)$ state at the S_1 minimum geometry, and the ~ 286.8 eV band to the 286.8 eV $C\ 1s \rightarrow \pi^*$ transition from the ${}^1B_{3u}(n\pi^*)$ state at the S_1 minimum geometry.

Looking now at the nitrogen K-edge in the gas phase (Fig. 2D), where the pre-edge is at 398.8 eV, a broad positive absorption band from ~ 393.6 to 395.2 eV is observed in the first ~ 50 fs before disappearing. Concurrently, positive absorption bands centered at ~ 395.3 eV, 396.4 eV, and 397.6 eV are emerging and show clear modulations in intensity. Looking above the pre-edge, there are two bands at 399.5 eV and 401 eV emerging at the same time as the others. These two above-pre-edge bands show clearer intensity modulations that are out of phase with each other.

At the nitrogen K-edge in solution phase (Fig. 2H), where the pre-edge is at 398.9 eV, a weak positive absorption band at ~ 396 eV appears initially before broadening into a broad band from ~ 394 to 396.2 eV at ~ 50 fs. After ~ 50 fs, this broad band narrows into two bands at ~ 395.2 eV and ~ 396.3 eV. Meanwhile, a strong absorption band at 397.8 eV emerges from time zero and plateaus around 100 fs. Above the edge, a weak band at ~ 400.3 eV starts emerging from time zero and merges into a broad peak from ~ 400 to 402 eV at ~ 70 fs.

At the nitrogen K-edge in the gas phase, based on the calculated spectra from Fig. 2B (and the schematics in Fig. S8), we can assign the broad ~ 393.6 to 395.2 eV band to the 395.2 eV $N\ 1s \rightarrow \pi$ [$1b_{1u} \rightarrow 1b_{2g}$ in the D_{2h} limit] transition from the

$^1B_{2u}(\pi\pi^*)$ state at the FC geometry, the ~ 395.3 eV band to the 395.5 eV N 1s \rightarrow n transition of the $^1B_{3u}(n\pi^*)$ state at the S_1 minimum geometry [$1b_{1u} \rightarrow 6a_g$ in D_{2h} , to a final core state of symmetry B_{2g}], the ~ 396.4 eV band to the 396.4 eV N 1s \rightarrow n transition of the $^1A_u(n\pi^*)$ state at the S_1 minimum geometry [also $1b_{1u} \rightarrow 6a_g$ in the D_{2h} limit, but to a final core state of symmetry B_{1g}], the ~ 397.6 eV band to the 397.6 eV N 1s $\rightarrow \pi^*$ [$1a_g \rightarrow 2b_{3u}(1\pi^*)$ in the D_{2h} limit, final core state A_g] transition from the $^1B_{3u}(n\pi^*)$ state at the S_1 minimum geometry, the ~ 399.5 eV band to the 399.2 eV N 1s $\rightarrow \pi^*$ transition from the $^1A_u(n\pi^*)$ state [also $1a_g \rightarrow 2b_{3u}(1\pi^*)$ in the D_{2h} limit, but to a final B_{3g} core state] at the S_1 minimum geometry, and the ~ 401 eV band to the 401 eV N 1s $\rightarrow \pi^*$ [$1b_{1u} \rightarrow 2b_{2g}(3\pi^*)$ in the D_{2h} limit] transition from the $^1B_{3u}(n\pi^*)$ state at the S_1 minimum geometry.

At the nitrogen K-edge in solution phase, based on the calculated spectra from Fig. 2F, we can assign the initial 396 eV band to a mix of the 396.1 eV N 1s $\rightarrow \pi$ transition from the $^1B_{2u}(\pi\pi^*)$ state at the FC geometry and 396.2 eV N 1s \rightarrow n transition of the $^1A_u(n\pi^*)$ state at the S_1 minimum geometry. The ~ 395.2 eV band is assigned to the 395.2 eV N 1s \rightarrow n transition from the $^1B_{3u}(n\pi^*)$ state, the ~ 397.8 eV band to the 397.7 eV N 1s $\rightarrow \pi^*$ transition from the $^1B_{3u}(n\pi^*)$ state at the S_1 minimum geometry, the ~ 400.3 eV band to the 399.4 eV N 1s $\rightarrow \pi^*$ transition from the $^1A_u(n\pi^*)$ state at the S_1 minimum geometry, and the ~ 402 eV band to the 401.5 eV N 1s $\rightarrow \pi^*$ ($3\pi^*$ in D_{2h}) transition from the $^1B_{3u}(n\pi^*)$ state at the S_1 minimum geometry.

The time dependence of these nitrogen K-edge differential absorbance bands over 150 fs is shown in Fig. 3, together with the calculated time-dependent populations (in Fig. 3A). These diabatic populations were obtained by projecting wave functions calculated along trajectories using the fewest-switches surface hopping (FSSH) method onto diabatic electronic wave functions defined at the ground-state minimum geometry [36]. These deep, counter-phased quantum beats indicate an efficient population transfer between the 1A_u and $^1B_{3u}$ states. The calculated spectral intensities corresponding to these FSSH calculations display the same trends as the population dynamics as shown in the SI (Fig. S21), where additional details on these calculations are provided. In gaseous pyrazine above the nitrogen pre-edge, the 399.5 and 401 eV bands (Fig. 3B) are fitted with the product of a step function and a cosine convoluted with a Gaussian of 30 fs full width at half maximum (FWHM). From peak to peak, the 401 eV band rises earlier than the 399.5 eV band by ~ 40 fs. It has two local maxima at ~ 40 fs and ~ 120 fs and a local minimum at ~ 70 fs, with a period of ~ 80 fs. The 399.5 eV band has local maxima at ~ 80 fs and ~ 150 fs and a local minimum at ~ 120 fs, with a period of ~ 70 fs. Given that the 399.5 and 401 eV bands are associated with dominant $^1A_u(n\pi^*)$ and $^1B_{3u}(n\pi^*)$ characters, respectively, the observed ΔOD quantum beats in the two bands reflect the electronic dynamics involving these two states. When fitted with a sigmoidal function convoluted with a cosine, both the 399.5 and 401 eV bands have a rise time of 50 ± 30 fs with a time constant of 30 ± 15 fs, and are nearly π out of phase with each other.

The experimentally observed quantum beat agrees well with the predictions of the gas-phase calculations shown in Fig. 3A. The red and green curves for $^1B_{3u}(n\pi^*)$ and $^1A_u(n\pi^*)$, respectively, are fitted with the product of a rising exponential and a

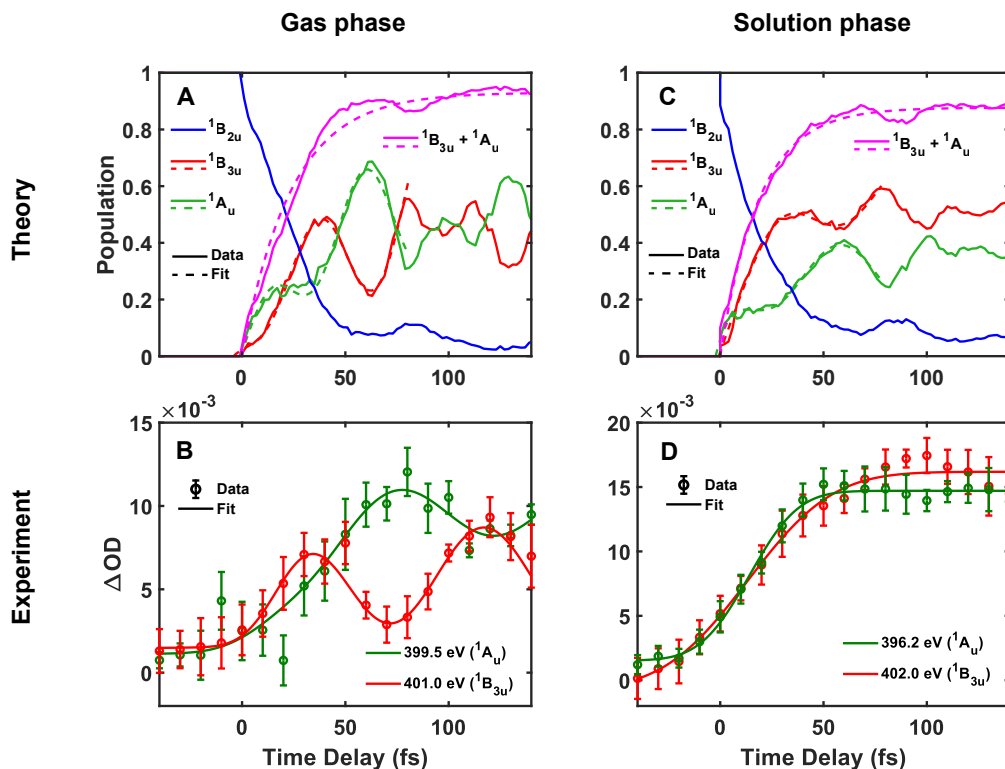


Fig. 3 Observation of electronic and vibrational dynamics in gas-phase pyrazine and their dephasing in aqueous solution (A, C) In gas phase and solution phase, respectively, populations of the diabatic ${}^1B_{2u}(\pi\pi^*)$, ${}^1B_{3u}(n\pi^*)$ and ${}^1A_u(n\pi^*)$ states based on FSSH trajectories. (B) Time-dependent ΔOD of gaseous pyrazine for the bands centered at 399.5 eV and 401.0 eV. According to calculations shown in Fig. 2B, these bands are associated with the ${}^1A_u(n\pi^*)$ and ${}^1B_{3u}(n\pi^*)$ characters, respectively. (D) Time-dependent ΔOD of 5M aqueous pyrazine for the bands centered at 396.2 eV and 402 eV. According to calculations shown in Fig. 2F, these bands are associated with the ${}^1A_u(n\pi^*)$ character and ${}^1B_{3u}(n\pi^*)$ characters, respectively. The error bars indicate the measured standard deviations over 12 and 9 sets of scans for gas and solution phase measurements, respectively.

cosine function, revealing that they are close to π out of phase with respect to each other. The brown curve for the summed populations of the ${}^1B_{3u}(n\pi^*)$ and ${}^1A_u(n\pi^*)$ states is fitted with a rising exponential function, yielding a time constant of 24.0 ± 1.2 fs.

At the nitrogen K-edge in aqueous pyrazine in Fig. 3D, the 396.2 and 402 eV bands, which are associated with the ${}^1A_u(n\pi^*)$ and ${}^1B_{3u}(n\pi^*)$ characters, respectively, do not display any visible quantum beats. These data were therefore fitted with sigmoidal functions. The 396.2 and 402 eV bands have rise times of 50 ± 20 fs and 80 ± 20 fs, respectively. As a caveat, it is worth mentioning that observation of pure ${}^1A_u(n\pi^*)/{}^1B_{3u}(n\pi^*)$ dynamics is prevented by overlap of three peaks at 396.2, 396.1 and 395.2 eV, which are assigned to transitions from the ${}^1A_u(n\pi^*)$, ${}^1B_{2u}(\pi\pi^*)$ and ${}^1B_{3u}(n\pi^*)$ states, respectively. Nevertheless, the absence of quantum beats in the 402.0 eV band is a reliable indicator of the lack of quantum beats in the solution phase. The calculations shown in Fig. 3C, which include two explicit water molecules and a conductor-like screening model (COSMO), do indeed predict a smaller (roughly by a factor of two) contrast of the quantum beat compared to

the isolated-molecule calculations (Fig. 3A). The complete suppression of the quantum beats in the experiment must therefore involve additional mechanisms, such as decoherence and dissipation, that go beyond those included in our simulations. The calculated rise time of the summed populations in solution phase is shorter than in the gas-phase calculations and amounts to 18.8 ± 0.6 fs.

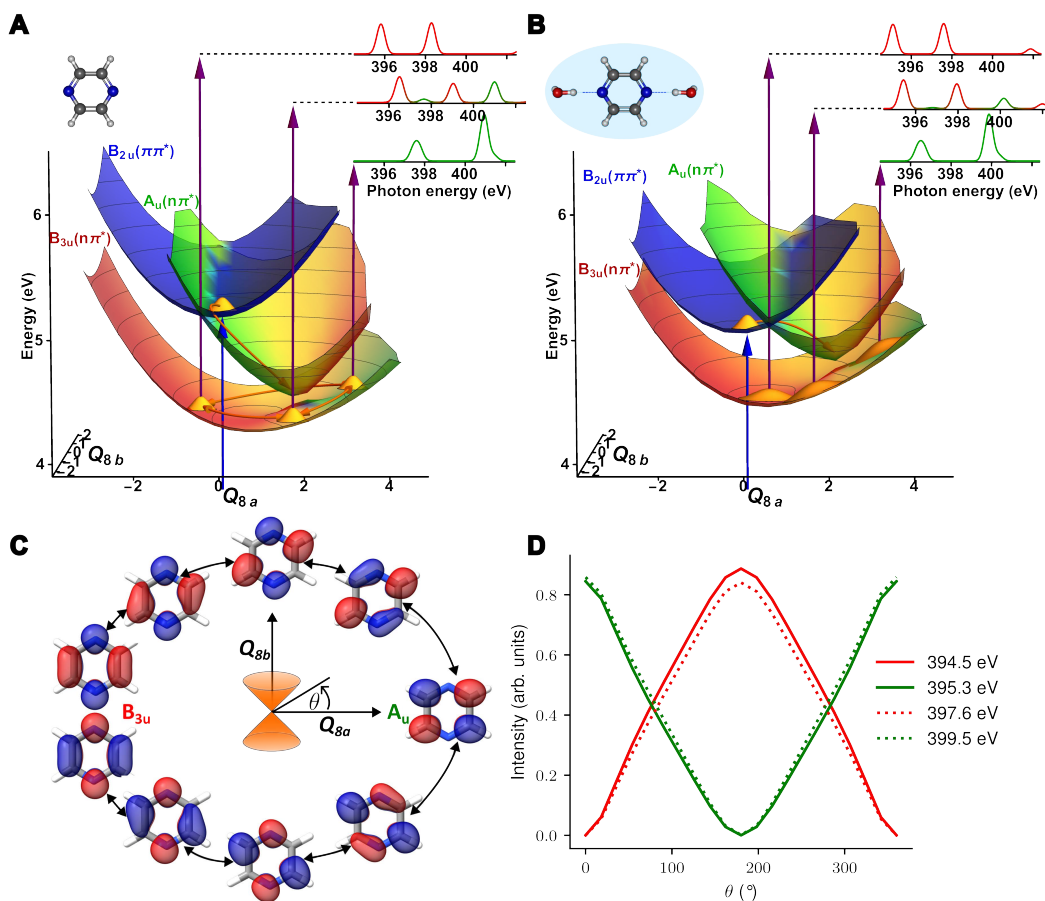


Fig. 4 Wavepacket dynamics in isolated and solvated pyrazine molecules. (A) Adiabatic potential-energy surfaces of the three lowest excited states of isolated pyrazine as a function of the Q_{8a} and Q_{8b} normal modes computed at the ADC(2)/aug-cc-pVDZ level of theory. Surfaces are colored according to contributions of ${}^1B_{3u}$, 1A_u and ${}^1B_{2u}$ electronic character in the wave functions of the excited states. (B) Same as (A) for the case of solvated pyrazine calculated with two explicit water molecules hydrogen-bonded to the nitrogen atoms and COSMO. Details of the calculations are given in the SI. (C) Particle NTOs for the S_1 state at geometries sampling a path around the conical intersection as indicated by arrows on the S_1 surfaces in (A). The colors of the isosurfaces encode the signs of the NTOs. (D) Relative intensities of absorption bands characteristic of the 1A_u (green) and ${}^1B_{3u}$ (red) states along a 2D circular path spanned by the Q_{8a} and Q_{8b} normal modes encircling the ${}^1B_{3u}/{}^1A_u$ CI.

We now discuss these new insights into the creation of electronic and vibrational dynamics in isolated and solvated pyrazine molecules in the light of the theoretical results. After photoexcitation to the ${}^1B_{2u}$ state, the molecular system moves away from the FC geometry in <30 fs following the slope of the excited-state potential-energy surface. This initial motion stabilizes all three excited states with respect to

the ground state and shifts the corresponding XA peaks. After this, we find that the positions of the bands remain fairly constant and, especially at the nitrogen K-edge, they are most easily assigned based on those calculated at the minimum of the S_1 state. Our experimental results obtained at both edges and in both phases of matter clearly show that both the $^1A_u(n\pi^*)$ and the $^1B_{3u}(n\pi^*)$ states are populated within a few tens of femtoseconds, creating electronic and vibrational dynamics in the gas phase that are suppressed in solution phase. The spectra obtained in solution phase are analogous to those from the gas phase, but with some notable differences. Peaks corresponding to the $^1A_u(n\pi^*)$ state appear to rise earlier than in the gas phase, likely due to $^1A_u/{}^1B_{2u}$ CI lying directly in the FC region, as a consequence of different solvation shifts of the two states.

To rationalize these findings, Fig. 4 displays the potential-energy surfaces of the relevant electronic states of isolated (A) and solvated (B) pyrazine. We chose the Q_{8a} and Q_{8b} modes since the $^1A_u/{}^1B_{3u}$ CI lies along the Q_{8a} mode, and the Q_{8b} mode is responsible for the coupling between these two states [19]. This is further confirmed by the fact that the population transfer is suppressed when the vibronic coupling mediated by the Q_{8b} mode is set to zero (Fig. S21). The Q_{8a} and Q_{8b} modes thus represent the pair of tuning and coupling modes, respectively, that are most relevant to the $^1A_u/{}^1B_{3u}$ dynamics. In the gas phase, the $^1B_{2u}/{}^1A_u$ CI is very close to the FC region, explaining the rapid population of both states. After crossing the $^1A_u/{}^1B_{3u}$ CI, electronic dynamics is created that involves both states in the gas phase and manifests itself in the observed quantum beats. Motion of the FSSH trajectories along these modes is shown in Fig. S20 and further analyzed in Figs. S21 and S22 by running MCTDH calculations on the potential-energy surfaces of Ref. [19].

The electronic dynamics underlying the observed quantum beats are illustrated in Fig. 4C, which shows the natural transition orbitals (NTOs) for the S_1 state at geometries sampling a closed path around the $^1B_{3u}/{}^1A_u$ CI. Following the evolution of the NTOs reveals their rotation around the aromatic ring of pyrazine reminiscent of a ring current. Ring currents in molecules have attracted considerable interest in recent years (Refs.[37–39], and references therein), but experimental evidence for such dynamics has been lacking. Although a uni-directional ring current cannot be generated in our experiment for symmetry reasons, the observed quantum beats can be interpreted as the consequence of a circular shift of the NTO around the aromatic ring. Our FSSH calculations indeed show that the excited-state trajectories can be grouped into two categories that encircle the $^1B_{3u}/{}^1A_u$ CI either clockwise or counter-clockwise (Fig. S20). The corresponding electronic dynamics are in excellent agreement with MCTDH calculations run on the same potential-energy surfaces (Fig. S21). The MCTDH calculations themselves provide a consistent picture by showing that the excited-state wavepacket splits in two components that encircle the CI either clockwise or counter-clockwise (Fig. S22). Overall, these results show that the electronic dynamics observed in this work corresponds to a circular rearrangement of the electronic structure around the aromatic ring of the molecule.

Our calculations additionally clarify why the observed electronic dynamics are directly accessible at the nitrogen K-edge. Whereas the NTO of the $^1B_{3u}$ state has large amplitude on the nitrogen atoms, that of the 1A_u state has none, providing an

intuitive interpretation why the observed quantum beats are out of phase and best visible at the nitrogen K-edge, as illustrated in Fig. 4D. The intensities in Fig. 4D are calculated along a tight circular path around the CI ($r = 0.1$ in dimensionless normal-mode coordinates), showing that they are indeed primarily sensitive to the electronic character. Finally, because of the geometric phase [40, 41], a closed loop around a CI is expected to result in a reversal of the signs of both the electronic and the nuclear wave functions, which is reflected in the phase of the NTOs shown in Fig. 4C, as well as in a node that appears in the nuclear wavepacket after its two components have encircled the CI in opposite directions (Fig. S22, [42]).

Turning to the role of solvation, our calculations show that solvation stabilizes the $\pi\pi^*$ state, whereas it destabilizes both of the $n\pi^*$ states. This finding has been qualitatively reproduced for a microsolvation model [43] (for details see section S3.3 of the SI) and is in agreement with solvation effects that were computationally found for nucleobases [44]. As Fig. 4 shows, the solvation effects on pyrazine thus change both the location of the CIs and their slopes. Solvation indeed moves the location of the ${}^1B_{2u}/{}^1A_u$ CI and causes a mixture of the two configuration characters near the FC point, explaining the earlier rise times of the corresponding bands in solution phase. Comparing the solvation effects on the two $n\pi^*$ states, we find that the 1A_u state is more destabilized by solvation than the ${}^1B_{3u}$ state. This leads to an energetic skew of the path on which the wave packet encircles the CI, contributing to the dephasing of the quantum beats. However, as mentioned above, our solution-phase calculations (shown in Figs. 3B and 4B) only partially account for solvation effects by including two explicit water molecules, hydrogen-bonded to the nitrogen atoms of pyrazine, and COSMO. Importantly, this partial account of solvation is nevertheless sufficient to reduce the contrast of the quantum beats by a factor of two as compared to the gas phase (Fig. 3A) and Fig. 3C identifies the differential solvation shifts as the likely origin of this partial dephasing. Since our experimental results show no discernible quantum beats, we conclude that additional mechanisms of decoherence and dissipation must be causing the observed complete dephasing on a time scale shorter than half of the 70-80 fs period of the observed quantum beats.

Our work shows that CI dynamics can create electronic dynamics that correspond to large-amplitude rearrangement of the electronic structure and simultaneously resolves a decades-old controversy regarding the electronic-relaxation pathway and dynamics of pyrazine.

Such electronic dynamics may be exploited for efficient long-range charge transfer [45] or for inducing very intense magnetic fields [37], enabling novel molecular functionalities. Turning to the solution-phase results, our study shows that solvation can lead to dephasing of electronic dynamics and change the time constants of electronic relaxation. Our dynamical calculations moreover show that effects beyond the solvation shifts of the electronic states, such as dissipation and decoherence, are responsible for the observed complete dephasing of the electronic dynamics within 40 fs. Our work thus quantifies the effects of complex fluctuating environments under ambient conditions on electronic and vibrational dynamics. Our study demonstrates a general approach to unraveling the impact of solvation on conical-intersection dynamics [14], which also includes the predicted creation of electronic coherences

at conical intersections [46] and exploring the applicability of the concepts of charge-directed reactivity [47, 48] on solution-phase dynamics.

Acknowledgments

We thank S. Gosh and A. Djorovic for supporting experiments on the ultraviolet absorbance of pyrazine solutions. We thank M. Moret, A. Schneider, M. Seiler for technical support. S.T. acknowledges discussion on solvent effects with Dr. B. Sharma, Prof. C. Hättig, and Prof. D. Marx, Ruhr-Universität Bochum.

Funding: We gratefully acknowledge funding from an ERC Consolidator Grant (Project No. 772797-ATTOLIQ), projects 200021_204844 (USCOBIX), 200021_172946 and 200020_204928, as well as the NCCR-MUST, funding instruments of the Swiss National Science Foundation. Z.Y. acknowledges financial support from an ETH Career Seed Grant No SEED-12 19-1/1-004952-00. B.N.C.T. acknowledges support from the European Union’s Horizon 2020 Research and Innovation Programme under the Marie Skłodowska-Curie Individual Fellowship (Grant Agreement 101027796). S.C. acknowledges the Independent Research Fund Denmark – Natural Sciences, DFF-RP2 Grant No. 7014-00258B. S.T. acknowledges funding from the Alexander von Humboldt Foundation under the Humboldt Research Fellowship (JPN 1201668 HFST-P). M.S. acknowledges funding from the Croatian Science Foundation (project IP-2020-02-9932). A.C.P. and H.K. acknowledge funding from the Research Council of Norway through FRINATEK (project No. 275506). We acknowledge computing resources from DeIC – Danish Infrastructure Cooperation (grant No. DeiC-DTU-N3-2023027), through UNINETT Sigma2–the National Infrastructure for High Performance Computing and Data Storage in Norway (project No. NN2962k) and through the Advanced computing service provided by University of Zagreb University Computing Centre - SRCE.

Author Contributions:

Y.-P.C., T.B., and Z.Y. carried out the experiments and analyzed the data. B.N.C.T., M.S., S.T., and S.C. carried out the CAS/RASPT2 calculations. A.C.P., S.C., and H.K. realized the CC calculations. M.S. realized the ADC(2) and the surface-hopping calculations. J.-P.W. and H.J.W. supervised the experimental work. S.C., H.K., and M.S. supervised the theoretical work. All authors discussed the data and contributed to the manuscript.

Competing interests

The authors declare no competing interests.

References

- [1] Drescher, M., Hentschel, M., Kienberger, R., Uiberacker, M., Yakolev, V., Scrinzi, A., Westerwalbesloh, T., Kleineberg, U., Krausz, F.: Time-resolved

- atomic innershell spectroscopy. *Nature* **419**, 803 (2002)
- [2] Klünder, K., Dahlström, J.M., Gisselbrecht, M., Fordell, T., Swoboda, M., Guénot, D., Johnsson, P., Caillat, J., Mauritsson, J., Maquet, A., Taïeb, L'Huillier, A.: Probing single-photon ionization on the attosecond time scale. *Phys. Rev. Lett.* **106**, 143002 (2011) <https://doi.org/10.1103/PhysRevLett.106.143002>
- [3] Calegari, F., Ayuso, D., Trabattoni, A., Belshaw, L., De Camillis, S., Anumula, S., Frassetto, F., Poletto, L., Palacios, A., Decleva, P., *et al.*: Ultrafast electron dynamics in phenylalanine initiated by attosecond pulses. *Science* **346**(6207), 336–339 (2014)
- [4] Kraus, P.M., Mignolet, B., Baykusheva, D., Rupenyan, A., Horný, L., Penka, E.F., Grassi, G., Tolstikhin, O.I., Schneider, J., Jensen, F., Madsen, L.B., Bandrauk, A.D., Remacle, F., Wörner, H.J.: Measurement and laser control of attosecond charge migration in ionized iodoacetylene. *Science* **350**, 790–795 (2015)
- [5] Wörner, H.J., Arrell, C.A., Banerji, N., Cannizzo, A., Chergui, M., Das, A.K., Hamm, P., Keller, U., Kraus, P.M., Liberatore, E., *et al.*: Charge migration and charge transfer in molecular systems. *Structural dynamics* **4**(6), 061508 (2017)
- [6] Matselyukh, D.T., Despré, V., Golubev, N.V., Kuleff, A.I., Wörner, H.J.: Decoherence and revival in attosecond charge migration driven by non-adiabatic dynamics. *Nature Physics* **18**(10), 1206–1213 (2022)
- [7] Engel, G.S., Calhoun, T.R., Read, E.L., Ahn, T.-K., Mančal, T., Cheng, Y.-C., Blankenship, R.E., Fleming, G.R.: Evidence for wavelike energy transfer through quantum coherence in photosynthetic systems. *Nature* **446**, 782–786 (2007)
- [8] Cao, J., Cogdell, R.J., Coker, D.F., Duan, H.-G., Hauer, J., Kleinekathöfer, U., Jansen, T.L., Mančal, T., Miller, R.D., Ogilvie, J.P., *et al.*: Quantum biology revisited. *Science Advances* **6**(14), 4888 (2020)
- [9] Gustin, I., Kim, C.W., McCamant, D.W., Franco, I.: Mapping electronic decoherence pathways in molecules. *Proceedings of the National Academy of Sciences* **120**(49), 2309987120 (2023) <https://doi.org/10.1073/pnas.2309987120> <https://arxiv.org/abs/https://www.pnas.org/doi/pdf/10.1073/pnas.2309987120>
- [10] Scholes, G.D., Fleming, G.R., Chen, L.X., Aspuru-Guzik, A., Buchleitner, A., Coker, D.F., Engel, G.S., Van Grondelle, R., Ishizaki, A., Jonas, D.M., *et al.*: Using coherence to enhance function in chemical and biophysical systems. *Nature* **543**(7647), 647–656 (2017)
- [11] Pertot, Y., Schmidt, C., Matthews, M., Chauvet, A., Huppert, M., Svoboda,

- V., Conta, A., Tehlar, A., Baykusheva, D., Wolf, J.-P., Wörner, H.J.: Time-resolved x-ray absorption spectroscopy with a water window high-harmonic source. *Science* **355**, 264–267 (2017) <https://doi.org/10.1126/science.aah6114>
- [12] Saito, N., Sannohe, H., Ishii, N., Kanai, T., Kosugi, N., Wu, Y., Chew, A., Han, S., Chang, Z., Itatani, J.: Real-time observation of electronic, vibrational, and rotational dynamics in nitric oxide with attosecond soft x-ray pulses at 400 eV. *Optica* **6**(12), 1542–1546 (2019)
- [13] Scutelnic, V., Tsuru, S., Pápai, M., Yang, Z., Epshtein, M., Xue, T., Haugen, E., Kobayashi, Y., Krylov, A.I., Møller, K.B., Coriani, S., Leone, S.R.: X-ray transient absorption reveals the $^1A_u(n\pi^*)$ state of pyrazine in electronic relaxation. *Nat. Commun.* **12**, 5003 (2021) <https://doi.org/10.1038/s41467-021-25045-0>
- [14] Zinchenko, K.S., Ardana-Lamas, F., Seidu, I., Neville, S.P., Veen, J., Lanfaloni, V.U., Schuurman, M.S., Wörner, H.J.: Sub-7-femtosecond conical-intersection dynamics probed at the carbon k-edge. *Science* **371**(6528), 489–494 (2021)
- [15] Schmidt, C., Pertot, Y., Balciunas, T., Zinchenko, K., Matthews, M., Wörner, H.J., Wolf, J.-P.: High-order harmonic source spanning up to the oxygen K-edge based on filamentation pulse compression. *Optics Express* **26**(9), 11834 (2018)
- [16] Werner, U., Mitrić, R., Suzuki, T., Bonačić-Koutecký, V.: Nonadiabatic dynamics within the time dependent density functional theory: Ultrafast photodynamics in pyrazine. *Chemical Physics* **349**(1-3), 319–324 (2008)
- [17] Kanno, M., Ito, Y., Shimakura, N., Koseki, S., Kono, H., Fujimura, Y.: Ab initio quantum dynamical analysis of ultrafast nonradiative transitions via conical intersections in pyrazine. *Physical Chemistry Chemical Physics* **17**(3), 2012–2024 (2015)
- [18] Mignolet, B., Kanno, M., Shimakura, N., Koseki, S., Remacle, F., Kono, H., Fujimura, Y.: Ultrafast nonradiative transition pathways in photo-excited pyrazine: Ab initio analysis of time-resolved vacuum ultraviolet photoelectron spectrum. *Chemical Physics* **515**, 704–709 (2018)
- [19] Sala, M., Lasorne, B., Gatti, F., Guérin, S.: The role of the low-lying dark $n\pi^*$ states in the photophysics of pyrazine: a quantum dynamics study. *Physical Chemistry Chemical Physics* **16**(30), 15957–15967 (2014)
- [20] Tsuru, S., Vidal, M.L., Pápai, M., Krylov, A.I., Møller, K.B., Coriani, S.: Time-resolved near-edge x-ray absorption fine structure of pyrazine from electronic structure and nuclear wave packet dynamics simulations. *The Journal of Chemical Physics* **151**(12), 124114 (2019)

- [21] Huang, X., Xie, W., Došlić, N., Gelin, M.F., Domcke, W.: Ab initio quasiclassical simulation of femtosecond time-resolved two-dimensional electronic spectra of pyrazine. *The Journal of Physical Chemistry Letters* **12**(48), 11736–11744 (2021)
- [22] Gelin, M.F., Huang, X., Xie, W., Chen, L., Došlić, N., Domcke, W.: Ab Initio Surface-Hopping Simulation of Femtosecond Transient-Absorption Pump–Probe Signals of Nonadiabatic Excited-State Dynamics Using the Doorway–Window Representation. *Journal of Chemical Theory and Computation* **17**(4), 2394–2408 (2021)
- [23] Freibert, A., Mendive-Tapia, D., Huse, N., Vendrell, O.: Femtosecond x-ray absorption spectroscopy of pyrazine at the nitrogen k-edge: on the validity of the lorentzian limit. *Journal of Physics B: Atomic, Molecular and Optical Physics* **54**(24), 244003 (2022)
- [24] Kaczun, T., Dempwolff, A.L., Huang, X., Gelin, M.F., Domcke, W., Dreuw, A.: Tuning UV Pump X-ray Probe Spectroscopy on the Nitrogen K Edge Reveals the Radiationless Relaxation of Pyrazine: Ab Initio Simulations Using the Quasiclassical Doorway–Window Approximation. *The Journal of Physical Chemistry Letters* **14**, 5648–5656 (2023)
- [25] Stert, V., Farmanara, P., Radloff, W.: Electron configuration changes in excited pyrazine molecules analyzed by femtosecond time-resolved photoelectron spectroscopy. *The Journal of Chemical Physics* **112**(10), 4460–4464 (2000)
- [26] Suzuki, T.: Femtosecond time-resolved photoelectron imaging. *Annu. Rev. Phys. Chem.* **57**, 555–592 (2006)
- [27] Horio, T., Fuji, T., Suzuki, Y.-I., Suzuki, T.: Probing ultrafast internal conversion through conical intersection via time-energy map of photoelectron angular anisotropy. *Journal of the American Chemical Society* **131**(30), 10392–10393 (2009)
- [28] Suzuki, Y.-I., Fuji, T., Horio, T., Suzuki, T.: Time-resolved photoelectron imaging of ultrafast $S_2 \rightarrow S_1$ internal conversion through conical intersection in pyrazine. *The Journal of Chemical Physics* **132**(17), 174302 (2010)
- [29] Horio, T., Spesyvtsev, R., Nagashima, K., Ingle, R.A., Suzuki, Y.-i., Suzuki, T.: Full observation of ultrafast cascaded radiationless transitions from S_2 ($\pi\pi^*$) state of pyrazine using vacuum ultraviolet photoelectron imaging. *The Journal of Chemical Physics* **145**(4), 044306 (2016)
- [30] Vall-Ilosera, G., Gao, B., Kivimaki, A., Coreno, M., Ruiz, J.A., Simone, M., Ågren, H., Rachlew, E.: The C 1s and N 1s near edge x-ray absorption fine structure spectra of five azabenzene in the gas phase (vol 128, artn 044316, 2008). *Journal of Chemical Physics* **128**(13), 044316 (2008)

- [31] Li Manni, G., Fdez. Galván, I., Alavi, A., Aleotti, F., Aquilante, F., Autschbach, J., Avagliano, D., Baiardi, A., Bao, J.J., Battaglia, S., *et al.*: The OpenMolcas Web: A Community-Driven Approach to Advancing Computational Chemistry. *Journal of Chemical Theory and Computation* **19**, 6933–6991 (2023)
- [32] Koch, H., Christiansen, O., Jørgensen, P., Sánchez de Merás, A.M., Helgaker, T.: The CC3 model: An iterative coupled cluster approach including connected triples. *J. Chem. Phys.* **106**(5), 1808–1818 (1997) <https://doi.org/10.1063/1.473322>
- [33] Christiansen, O., Koch, H., Jørgensen, P.: Response functions in the CC3 iterative triple excitation model. *J. Chem. Phys.* **103**(17), 7429–7441 (1995) <https://doi.org/10.1063/1.470315>
- [34] Folkestad, S.D., Kjørstad, E.F., Myhre, R.H., Andersen, J.H., Balbi, A., Coriani, S., Giovannini, T., Goletto, L., Haugland, T.S., Hutcheson, A., *et al.*: e^T 1.0: An open source electronic structure program with emphasis on coupled cluster and multilevel methods. *The Journal of Chemical Physics* **152**(18), 184103 (2020)
- [35] Paul, A.C., Myhre, R.H., Koch, H.: New and efficient implementation of CC3. *Journal of Chemical Theory and Computation* **17**(1), 117–126 (2020)
- [36] Piteša, T., Sapunar, M., Ponzi, A., Gelin, M.F., Došlić, N., Domcke, W., Decleva, P.: Combined surface-hopping, dyson orbital, and b-spline approach for the computation of time-resolved photoelectron spectroscopy signals: The internal conversion in pyrazine. *Journal of Chemical Theory and Computation* **17**(8), 5098–5109 (2021)
- [37] Barth, I., Manz, J., Shigeta, Y., Yagi, K.: Unidirectional electronic ring current driven by a few cycle circularly polarized laser pulse: quantum model simulations for mg- porphyrin. *Journal of the American Chemical Society* **128**(21), 7043–7049 (2006)
- [38] Mineo, H., Lin, S., Fujimura, Y.: Coherent π -electron dynamics of (p)-2, 2'-biphenol induced by ultrashort linearly polarized uv pulses: Angular momentum and ring current. *The Journal of Chemical Physics* **138**(7) (2013)
- [39] Yuan, K.-J., Shu, C.-C., Dong, D., Bandrauk, A.D.: Attosecond dynamics of molecular electronic ring currents. *The Journal of Physical Chemistry Letters* **8**(10), 2229–2235 (2017)
- [40] Longuet-Higgins, H.C., Öpik, U., Pryce, M.H.L., Sack, R.: Studies of the jahn-teller effect. ii. the dynamical problem. *Proceedings of the Royal Society of London. Series A. Mathematical and Physical Sciences* **244**(1236), 1–16 (1958)

- [41] Berry, M.V.: Quantal phase factors accompanying adiabatic changes. *Proceedings of the Royal Society of London. A. Mathematical and Physical Sciences* **392**(1802), 45–57 (1984)
- [42] Duan, H.-G., Qi, D.-L., Sun, Z.-R., Miller, R.D., Thorwart, M.: Signature of the geometric phase in the wave packet dynamics on hypersurfaces. *Chemical Physics* **515**, 21–27 (2018)
- [43] Tsuru, S., Sharma, B., Marx, D., Hättig, C.: Structural sampling and solvation models for the simulation of electronic spectra: Pyrazine as a case study. *Journal of Chemical Theory and Computation* **19**(8), 2291–2303 (2023) <https://doi.org/10.1021/acs.jctc.2c01129>
- [44] Improta, R., Santoro, F., Blancafort, L.: Quantum mechanical studies on the photophysics and the photochemistry of nucleic acids and nucleobases. *Chemical reviews* **116**(6), 3540–3593 (2016)
- [45] Falke, S.M., Rozzi, C.A., Brida, D., Maiuri, M., Amato, M., Sommer, E., De Sio, A., Rubio, A., Cerullo, G., Molinari, E., Lienau, C.: Coherent ultrafast charge transfer in an organic photovoltaic blend. *Science* **344**(6187), 1001–1005 (2014) <https://doi.org/10.1126/science.1249771>
- [46] Kowalewski, M., Bennett, K., Dorfman, K.E., Mukamel, S.: Catching conical intersections in the act: Monitoring transient electronic coherences by attosecond stimulated x-ray raman signals. *Phys. Rev. Lett.* **115**(19), 193003 (2015)
- [47] Remacle, F., Levine, R., Ratner, M.A.: Charge directed reactivity: a simple electronic model, exhibiting site selectivity, for the dissociation of ions. *Chemical physics letters* **285**(1-2), 25–33 (1998)
- [48] Yin, Z., Chang, Y.-P., Balčiūnas, T., Shakya, Y., Djorovic, A., Geoffrey, G., Fazio, G., Santra, R., Inhester, L., Wolf, J.-P., Wörner, H.J.: Femtosecond proton transfer in urea solutions probed by x-ray spectroscopy. *Nature* **619**(7971), 749–754 (2023)
- [49] Yin, Z., Peters, H.B., Hahn, U., Agåker, M., Hage, A., Reininger, R., Siewert, F., Nordgren, J., Viehhaus, J., Techert, S.: A new compact soft x-ray spectrometer for resonant inelastic x-ray scattering studies at PETRA III. *Review of Scientific Instruments* **86**(9), 093109 (2015) <https://doi.org/10.1063/1.4930968>
- [50] Smith, A.D., Balciunas, T., Chang, Y.-P., Schmidt, C., Zinchenko, K., Nunes, F.B., Rossi, E., Svoboda, V., Yin, Z., Wolf, J.-P., Wörner, H.J.: Femtosecond soft-x-ray absorption spectroscopy of liquids with a water-window high-harmonic source. *The Journal of Physical Chemistry Letters* **11**(6), 1981–1988 (2020)

- [51] Yin, Z., Luu, T.T., Wörner, H.J.: Few-cycle high-harmonic generation in liquids: in-operando thickness measurement of flat microjets. *Journal of Physics: Photonics* **2**(044007) (2020)
- [52] Luu, T.T., Yin, Z., Jain, A., Gaumnitz, T., Pertot, Y., Ma, J., Wörner, H.J.: Extreme-ultraviolet high-harmonic generation in liquids. *Nature Communications* **9**(1), 3723 (2018) <https://doi.org/10.1038/s41467-018-06040-4>
- [53] Battaglia, S., Fransén, L., Fdez. Galván, I., Lindh, R.: Regularized CASPT2: an Intruder-State-Free Approach. *J. Chem. Theory Comput.* **18**(8), 4814–4825 (2022)

Methods

Experimental Setup

The primary light source of this experiment is a Ti:Sapphire regenerative amplifier providing 4 mJ pulses that are subsequently amplified in a cryogenically-cooled two-pass amplifier. The two-stage Ti:Sapphire-based laser system provides 17 mJ, ~ 30 fs pulses at 1 kHz repetition rate. 90% of the output is used to pump a BBO-based type-II parametric amplifier seeded with a white-light supercontinuum originating from the same pump pulse. The parametric amplifier delivers ~ 1.6 mJ, ~ 30 fs idler pulses centered at $\lambda = 1.8 \mu\text{m}$ wavelength that are passively carrier-envelope-phase (CEP) stabilized. This mid-IR output is then compressed down to sub-three-cycle pulses in a dual-filamentation setup to ~ 12 fs [15]. The compressed pulses are then focused by a $f = 250$ mm spherical mirror into a high-pressure He gas cell where the broadband soft X-ray probe is generated and focused via a toroidal mirror with a focal spot size of $\sim 62 \mu\text{m}$ on the sub- μm liquid flat-jet. The passing beam is then diffracted on a flat-field varied-line-spacing (VLS) grating on a 2D CCD soft X-ray camera from Andor. The energy resolution of the soft X-ray VLS spectrometer is around 0.3 eV and 0.4 eV on the carbon and nitrogen K-edges, respectively [49]. The other 10% of the initial 800 nm beam is triple frequency doubled via BBO crystals to create 266 nm pump pulses. The pump pulses were characterized using self-diffraction frequency-resolved optical gating (FROG), which provided a measured pulse length of around ~ 30 fs, which is dominating the overall experimental time resolution. The pump pulse travel distance is matched with the beam path length of the probe and a high precision delay stage varies the time delays. Two $100 \mu\text{m}$ Ti filters were used to filter out the mid-IR beam from the HHG and also for differential pumping between the spectrometer and the experimental interaction chamber. Additional details on the experimental setup can be found in Ref. [50]. For both gaseous and aqueous phase measurements, the error bars are the measured standard deviations over 12 and 9 sets of scans, respectively, each having 20 spectra for each time delay and every spectra having an exposure time of 4s (given a laser repetition rate of 1 kHz).

Sample-Delivery Systems

To generate the sub- μm liquid flat-jet, we utilized two cylindrical jets with an orifice of $\sim 20 \mu\text{m}$ and let them collide under a specific angle of 48 deg. The home-built sample-delivery device allows thickness within hundreds of nm thickness as measurements showed [51]. A more detailed description of the flat jet system and its properties can be found in Refs. [51, 52]. Aqueous solutions of 5M pyrazine were used for the solution phase measurements and were freshly prepared on each day. For the gas-phase experiment, a heating device was designed to evaporate the crystalline pyrazine samples into the gas phase at $\sim 51 \text{ }^\circ\text{C}$, just below its melting point. This was done in the experimental chamber to avoid condensation on the way. The gas sample was then guided into a metallic cuvette with ca. 1 mm thickness.

Theoretical Methods

To assign the peaks in the experimental spectra, electronic structure calculations were conducted at the level of regularized multi-state restricted-active-space second-order perturbation theory [53] RASPT2/RAS2(10e,8o) for both the initial and final states of core excitations. The population dynamics was investigated by nonadiabatic dynamics simulation in the fewest-switches surface hopping (FSSH) scheme based on ADC(2)/aug-cc-pVDZ. Time-resolved differential absorbance spectra were constructed using the nuclear ensemble approach by calculating XAS spectra for an ensemble of geometries sampled from FSSH trajectories.

In the RASPT2 calculations, RAS2 consisted of the two n_{N} , three π and three π^* orbitals. The RAS1 space contained all the carbon and nitrogen 1s orbitals in the spectral simulations at the carbon and nitrogen K-edges, respectively. The RAS1 space was fully occupied in the initial states (ground state or valence excited states). The final core excited states were obtained by enforcing single electron occupation in RAS1 using the HEXS projection technique available in OpenMOLCAS [31], and thus the molecular orbitals in the core excited states were optimized under the presence of core hole in RAS1. In the solution-phase calculations, the solvent effects were considered by embedding the pyrazine molecule in PCM. The peak assignments based on RASPT2 were confirmed by calculating the core excitation energies and oscillator strengths with CC3 and CCSDT.

The 170 and 187 initial conditions of the FSSH simulation were randomly prepared in the 4.56-4.92 eV energy window, which corresponded to the low-energy part of the second absorption band in UV-Vis absorption, in the gas and aqueous-solution phases, respectively. Solvent effects were considered by including two explicit water molecules and COSMO in the aqueous solution phase. Each trajectory was propagated with a timestep of 0.5 fs up to 200 fs.

Further details concerning the calculations, including a more exhaustive list of references to the methods utilized, are given in the SI.

Data Availability

The datasets generated during and/or analyzed during the current study are available from the corresponding author on reasonable request.

Supporting Information for Electronic dynamics created at conical intersections and its dephasing in aqueous solution

Yi-Ping Chang^{1,2†}, Tadas Balciunas^{1,3†}, Zhong Yin^{3,4*†}, Marin Sapunar^{5†}, Bruno N. C. Tenorio^{6,7†}, Alexander C. Paul^{8†}, Shota Tsuru^{9,10}, Henrik Koch^{8*}, Jean–Pierre Wolf^{1*}, Sonia Coriani^{6*} and Hans Jakob Wörner^{3*}

¹GAP–Biophotonics, Université de Genève, 1205 Geneva, Switzerland.

²European XFEL, 22689 Schenefeld, Germany.

³Laboratory of Physical Chemistry, ETH Zürich, 8093 Zürich, Switzerland.

⁴International Center for Synchrotron Radiation Innovation Smart, Tohoku University, 980-8577 Sendai, Japan.

⁵Division of Physical Chemistry, Ruđer Bošković Institute, 10000 Zagreb, Croatia.

⁶Department of Chemistry, Technical University of Denmark, 2800 Kongens Lyngby, Denmark.

⁷Instituto Madrileño de Estudios Avanzados en Nanociencia, IMDEA–Nanociencia, 28049 Madrid, Spain.

⁸Department of Chemistry, Norwegian University of Science and Technology, 7034 Trondheim, Norway.

⁹Lehrstuhl für Theoretische Chemie, Ruhr-Universität Bochum, 44801 Bochum, Germany.

¹⁰RIKEN Center for Computational Science, RIKEN, 650-0047 Kobe, Japan.

*Corresponding author(s). E-mail(s): yinz@tohoku.ac.jp; henrik.koch@ntnu.no; jean-pierre.wolf@unige.ch; soco@kemi.dtu.dk; hwoerner@ethz.ch;

†These authors contributed equally to this work.

Contents

1	Additional Transient-Absorption Data	2
1.1	Time-dependence of differential absorbance at the nitrogen K-edge . . .	3
1.2	Depletion-corrected spectra	3
1.3	Pump-probe scans extending to delays of 2 ps	3
2	Theoretical Methods	9
2.1	Symmetry analysis at the FC geometry (D_{2h} symmetry)	11
2.2	RASPT2 calculations	13
2.3	CCSD and CC3 calculations	14
2.4	Comparison of static CC3 and RASPT2 spectra with experiment at the Carbon and Nitrogen K-edges	20
2.5	Nuclear dynamics	22
2.5.1	Simulated UV spectra	22
2.5.2	Fewest-Switches Surface Hopping calculations	23
2.5.3	Comparing FSSH and MCTDH calculations	24
2.6	Simulated TR-XAS	28
3	Interpretation of the solvent effects	31
3.1	Concentration-dependent absorption spectra	31
3.2	Self-association effect	32
3.3	Solvent effects in each excited state	34

1 Additional Transient-Absorption Data

Time-dependence of differential absorbance at the carbon K-edge

The time dependence of these carbon K-edge differential absorbance bands is shown in Fig. S1. In gaseous pyrazine, the 281.3-eV band is fitted with a convolution of the gaussian instrument-response function with an exponential decay function $e^{-t/\tau}$ and the 282.3-eV band with a sigmoidal function, as shown in Fig. S1A. The 281.3-eV band, associated with the ${}^1B_{2u}(\pi\pi^*)$ character, has a time constant of 120 ± 20 fs. The 282.3 eV band, which is associated with mixed ${}^1B_{3u}(n\pi^*)$ and ${}^1A_u(n\pi^*)$ character, has a rise time of 70 ± 20 fs.

The 284.2-eV and 287.2-eV bands (Fig. S1C) are both fitted with sigmoidal functions convoluted with cosines. The 284.2-eV band, which is associated with the ${}^1A_u(n\pi^*)$ character, has a rise-time of 130 ± 40 fs with a time constant of 70 ± 20 fs in the first 150 fs. The 287.2-eV band, which is associated with the ${}^1B_{3u}(n\pi^*)$ character, has a rise-time of 90 ± 40 fs with a time constant of 50 ± 20 fs, and emerges earlier than the 284.2-eV band by 20 ± 10 fs. The two bands also show weak out-of-phase oscillations.

In aqueous pyrazine, again the 281.3 eV is fitted with a convolution of the gaussian instrument response function with an exponential decay function $e^{-t/\tau}$ and the 281.9 eV band with a sigmoid function, as shown in Fig. S1B. The 281.3 eV band, which is associated with the ${}^1B_{2u}(\pi\pi^*)$ character, has a time constant of 130 ± 40 fs.

The 281.9 eV band, which is associated with mixed $^1B_{3u}(n\pi^*)$ and $^1A_u(n\pi^*)$ character, has a rise time of 50 ± 20 fs. For the 284.4 and 286.8 eV bands (Fig. S1D), they are fitted with a sigmoidal function and an IRF convoluted with an exponential decay, respectively. The 284.4 eV band, which is associated with the $^1A_u(n\pi^*)$ character, has a rise-time of 70 ± 10 fs in the first 100 fs but starts declining in intensity afterward. The 286.8 eV band, which is associated with the $^1B_{3u}(n\pi^*)$ character, has a time constant of 140 ± 40 fs.

1.1 Time-dependence of differential absorbance at the nitrogen K-edge

Looking below the nitrogen pre-edge in gas phase, we have the polynomial fits of 395.3, 396.4 and 397.6 eV bands in Fig. S2A, with character $^1B_{3u}(n\pi^*)$, $^1A_u(n\pi^*)$ and $^1B_{3u}(n\pi^*)$, respectively. These below-edge bands show weaker but still qualitatively comparable oscillations compared to the above-edge bands, showing a contrast in ΔOD intensities near ~ 90 fs. The weaker oscillations is likely due to a greater overlap of transition peaks below the pre-edge than above the pre-edge (Fig. 2B in the manuscript). Averaging all three of these bands together and fitting them with a sigmoid gives a rise time of 70 ± 40 fs.

Above the nitrogen pre-edge in aqueous pyrazine in Fig. S2B, the 397.8 eV and 400.3 eV bands, which are associated with the $^1B_{3u}(n\pi^*)$ and $^1A_u(n\pi^*)$ characters, respectively, do not display any visible oscillations. From sigmoidal function fits, the 397.8 and 400.3 eV bands have rise times of 90 ± 20 fs and 90 ± 50 fs, respectively.

1.2 Depletion-corrected spectra

This section presents depletion-corrected spectra at the carbon K-edge (Fig. S3) and the nitrogen K-edge (Fig. S4). These spectra were obtained by adding the ground-state spectra (blue shaded areas) scaled by the excitation fraction to the measured ΔOD spectra at positive time delays. The excitation fraction was determined in each measurement by applying a positivity constraint to the depletion corrected spectra.

1.3 Pump-probe scans extending to delays of 2 ps

Measurements were also performed for the initial 2 ps delay range. These are shown in Fig. S5 with mostly similar bands to the initial 150 fs measurements.

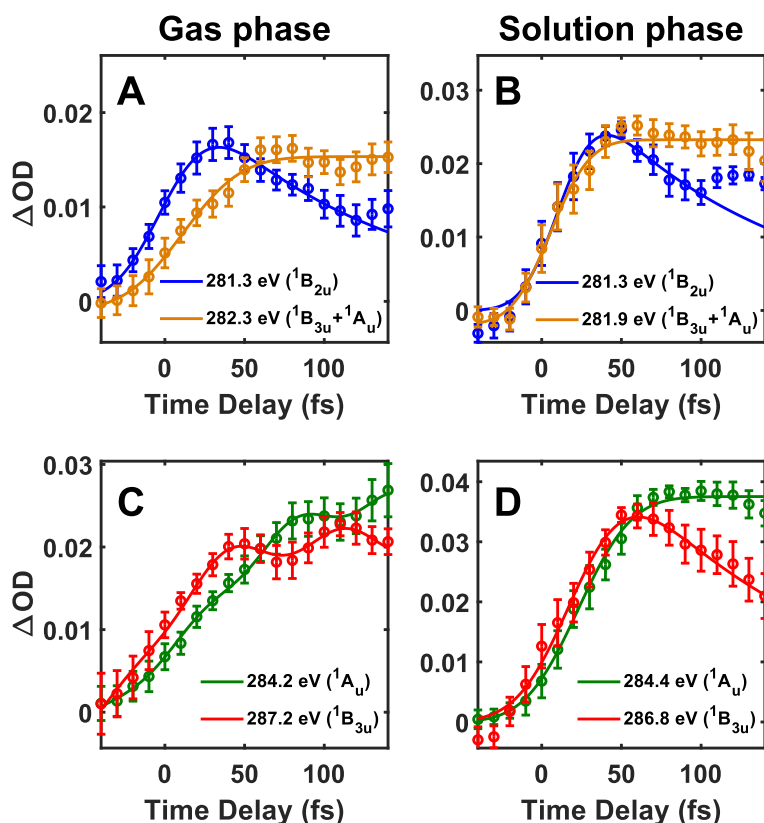


Fig. S1: Time dependence of the differential absorbance bands at the carbon K-edge. (A) Lineouts at the carbon K-edge of gaseous pyrazine for the 281.3 and 282.3 eV bands. According to calculations shown in Fig. S3A, the 281.3 band is associated with the ${}^1B_{2u}(\pi\pi^*)$ character, and the 282.3 eV band with mixed ${}^1B_{3u}(n\pi^*)$ and ${}^1A_u(n\pi^*)$ characters, respectively. (B) Lineouts at the carbon K-edge of 5M aqueous pyrazine for 281.3 and 281.9 eV bands. According to calculations shown in Fig. S3B, the 281.3 band is associated with the ${}^1B_{2u}(\pi\pi^*)$ character, and the 281.9 eV band with mixed ${}^1B_{3u}(n\pi^*)$ and ${}^1A_u(n\pi^*)$ characters, respectively. (C) Lineouts at the carbon K-edge of gaseous pyrazine for 284.2 and 287.2 eV bands. According to calculations shown in Fig. S3A, the 284.2 and 287.2 eV bands are associated with the ${}^1A_u(n\pi^*)$ and ${}^1B_{3u}(n\pi^*)$ characters, respectively. The 284.2 eV band has an earlier rise-time than the 287.2 eV band and the two bands show weak out-of-phase oscillations. (D) Lineouts at the carbon K-edge of 5M aqueous pyrazine for 284.4 and 286.8 eV bands. According to calculations shown in Fig. S3B, the 284.4 eV band is associated with the ${}^1A_u(n\pi^*)$ character, while the 286.8 eV band is associated with the ${}^1B_{3u}(n\pi^*)$ character.

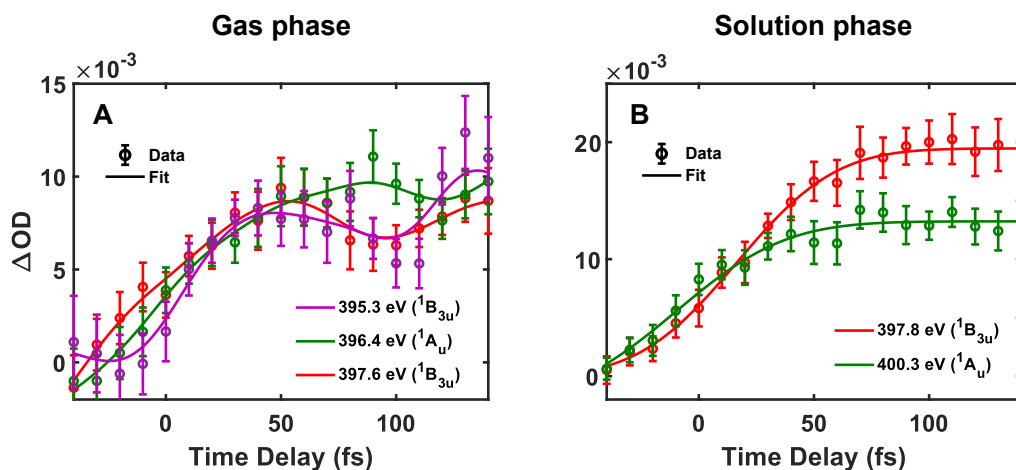


Fig. S2: (A,B) Time dependence of differential absorbance bands at the nitrogen K-edge over 150 fs. (A) Lineouts at the nitrogen K-edge of gaseous pyrazine for 395.3, 396.4 and 397.6 eV bands. According to calculations shown in Fig. S4A, the 395.3, 396.4 and 397.6 eV bands are associated with the ${}^1B_{3u}(n\pi^*)$, ${}^1A_u(n\pi^*)$ and ${}^1B_{3u}(n\pi^*)$ characters, respectively. (B) Lineouts at the nitrogen K-edge of 5M aqueous pyrazine for 397.8 eV and 400.3 eV bands. According to calculations shown in Fig. S4B, the 397.8 eV and 400.3 eV bands are associated with the ${}^1B_{3u}(n\pi^*)$ and ${}^1A_u(n\pi^*)$ characters, respectively.

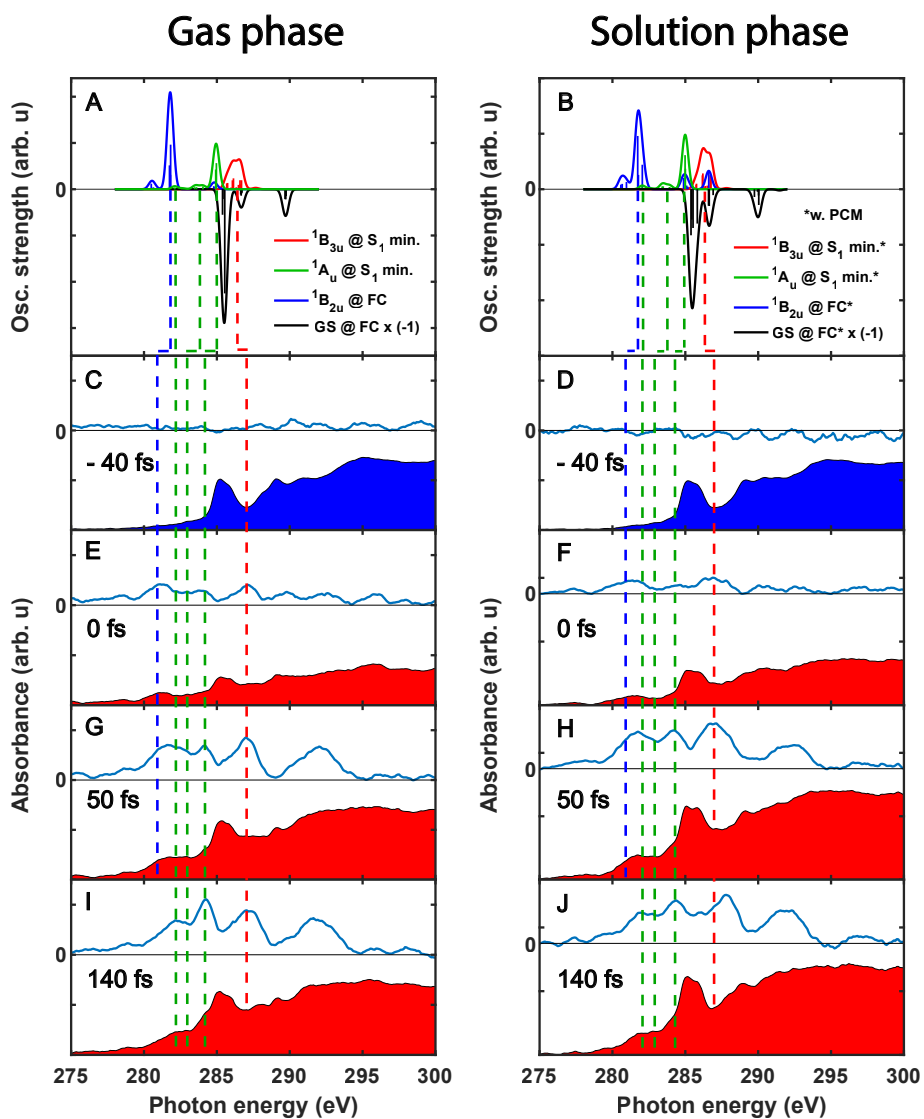


Fig. S3: (A),(B) carbon K-edge excited-state XA spectra calculated at the RASPT2/RAS2(10e,8o) level at both the FC and relaxed geometries for the first valence-excited state (S_1), with and without PCM, respectively. Differential absorbance spectra (blue lines) and ground state depletion-corrected spectra (shaded areas) at the carbon K-edge of gaseous pyrazine ((C),(E),(G),(I)) and 5M aqueous pyrazine ((D),(F),(H),(J)) at different time delays of -40 fs, 0 fs, 50 fs, and 140 fs. The pure ground state spectra are shown by the blue-shaded areas at -40 fs and the depletion-corrected spectra by red-shaded areas at later delays.

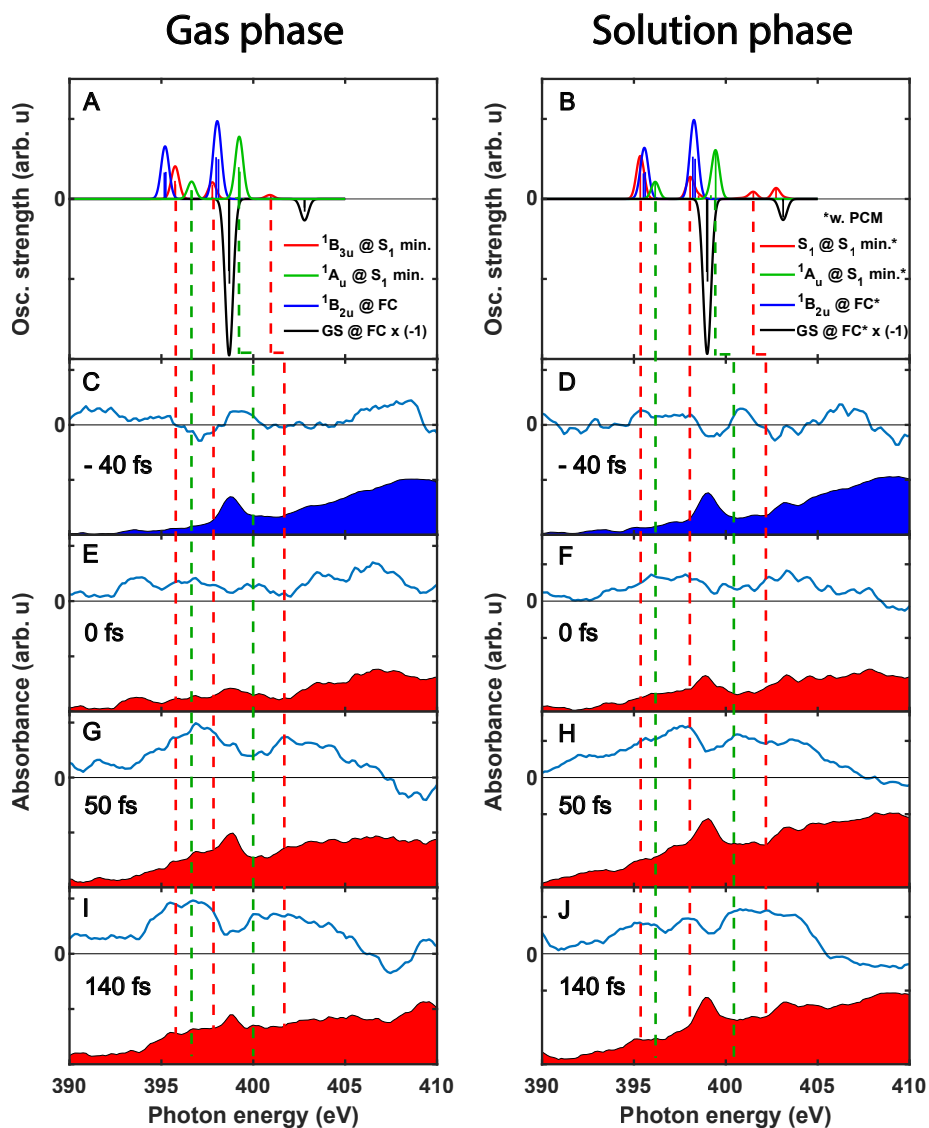


Fig. S4: (A),(B) Nitrogen K-edge excited-state XA spectra calculated at the RASPT2/RAS2(10e,8o) level at both the FC and relaxed geometries for the first valence excited state (S_1), with and without PCM, respectively. Differential absorbance spectra (blue lines) and ground state depletion-corrected spectra (shaded areas) at the nitrogen K-edge of gaseous pyrazine ((C),(E),(G),(I)) and 5M aqueous pyrazine ((D),(F),(H),(J)) at different time delays of -40 fs, 0 fs, 50 fs and 140 fs. The pure ground state spectra are shown by the blue-shaded areas at -40 fs and the depletion-corrected spectra by red-shaded areas at later delays.

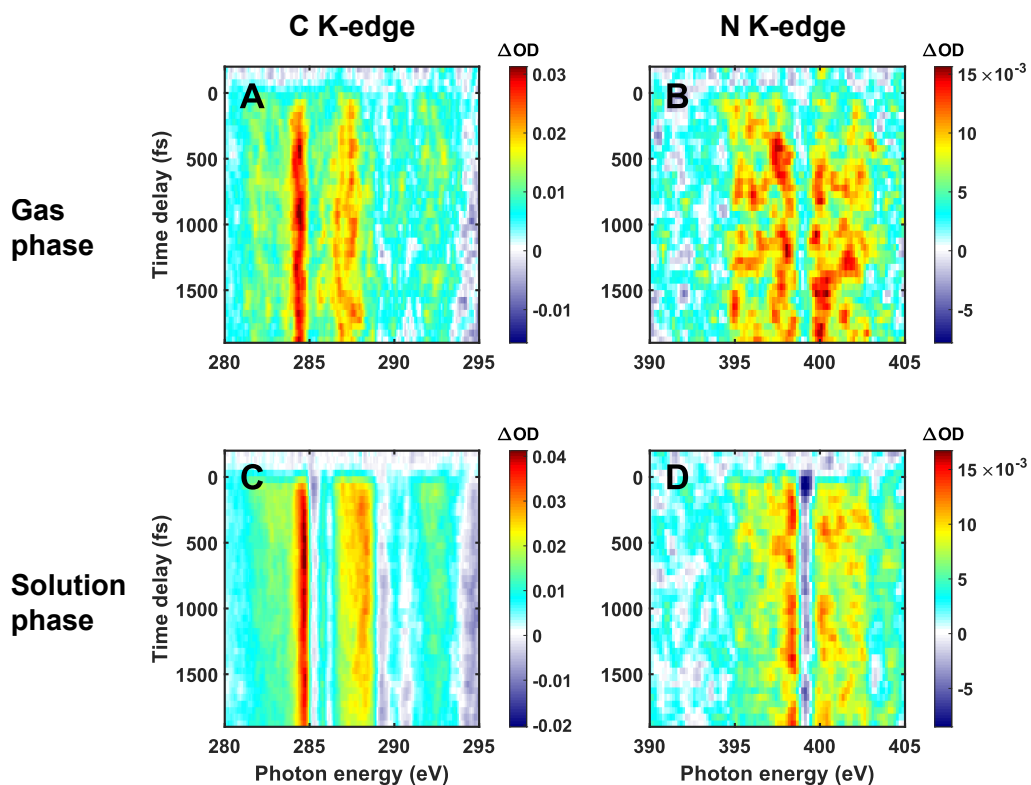


Fig. S5: Time-resolved differential absorbance spectra of pyrazine over the initial ~ 2 ps. (A,B) Time-resolved differential absorbance spectra at the carbon and nitrogen K-edges of gaseous pyrazine, respectively. (C,D) Time-resolved differential absorbance spectra at the carbon and nitrogen K-edges of 5M aqueous pyrazine, respectively. These solution-phase data have been recorded with a ~ 2 times higher pump intensity compared to the data shown in Fig. 2G,H of the main text.

2 Theoretical Methods

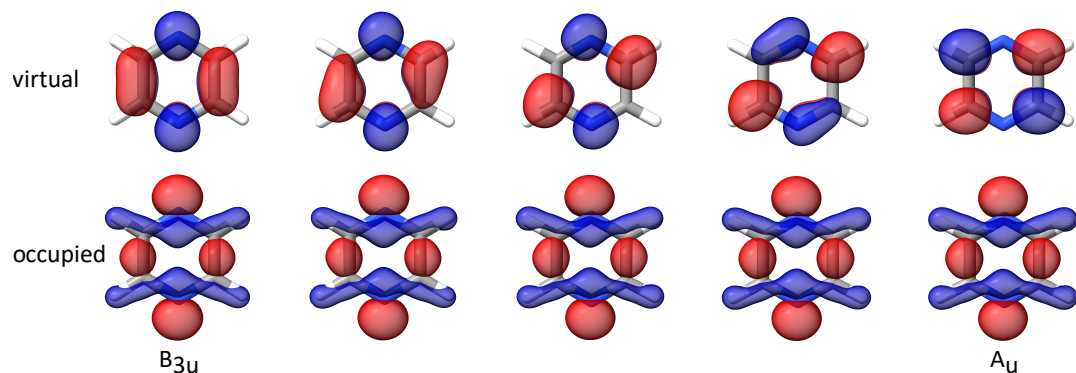


Fig. S6: NTOs for the S_1 state at geometries along a path from a geometry where S_1 can be assigned to B_{3u} to a geometry where the S_1 state can be assigned to A_u symmetry. The geometries used are part of a PES scan utilized to prepare Fig. 4. The scan is a path around the conical intersection as indicated by the arrows on the S_1 surface in Fig. 4. The potential is symmetric and therefore completing the cycle is just mirroring the plot, as shown in Fig. 4 of the main text.

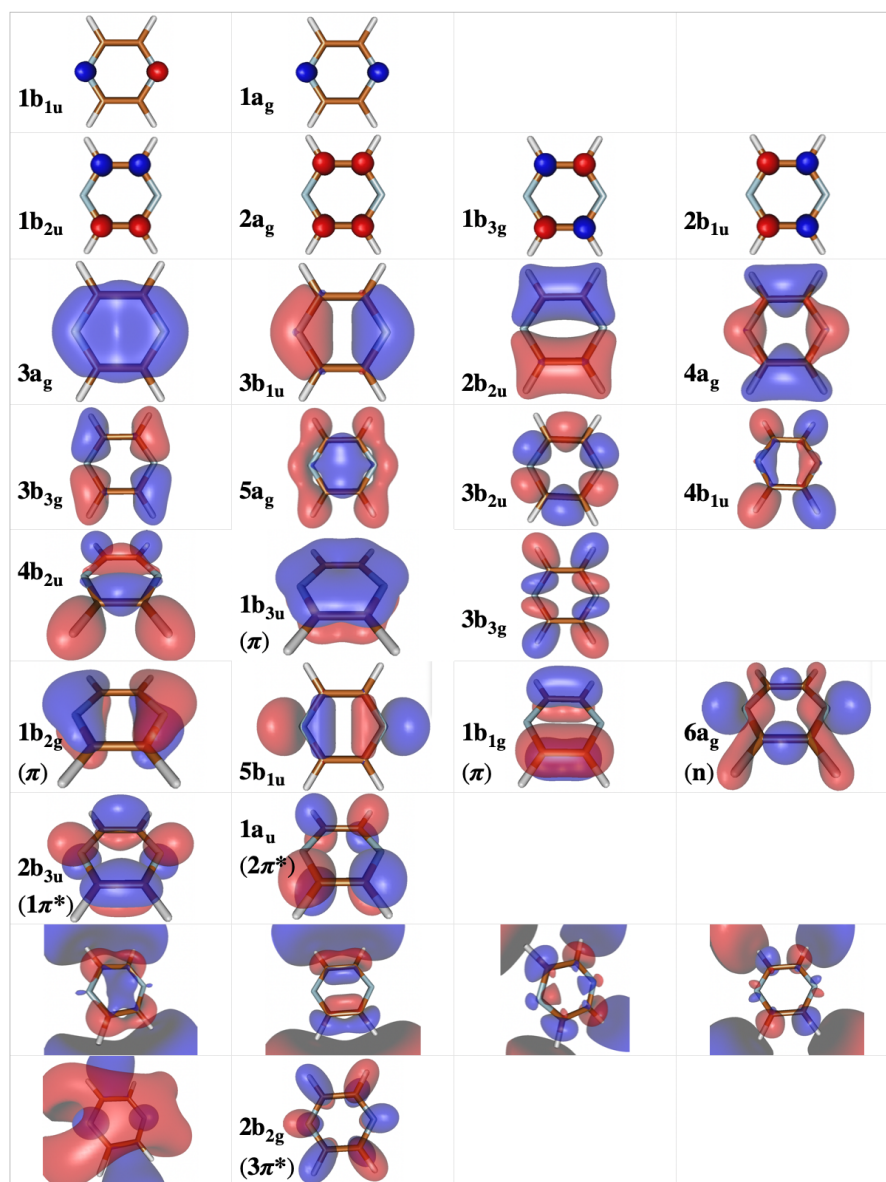


Fig. S7: Occupied molecular orbitals and first virtual orbitals of pyrazine (CAMB3LYP/cc-pVTZ). Mulliken symmetry notation.

2.1 Symmetry analysis at the FC geometry (D_{2h} symmetry)

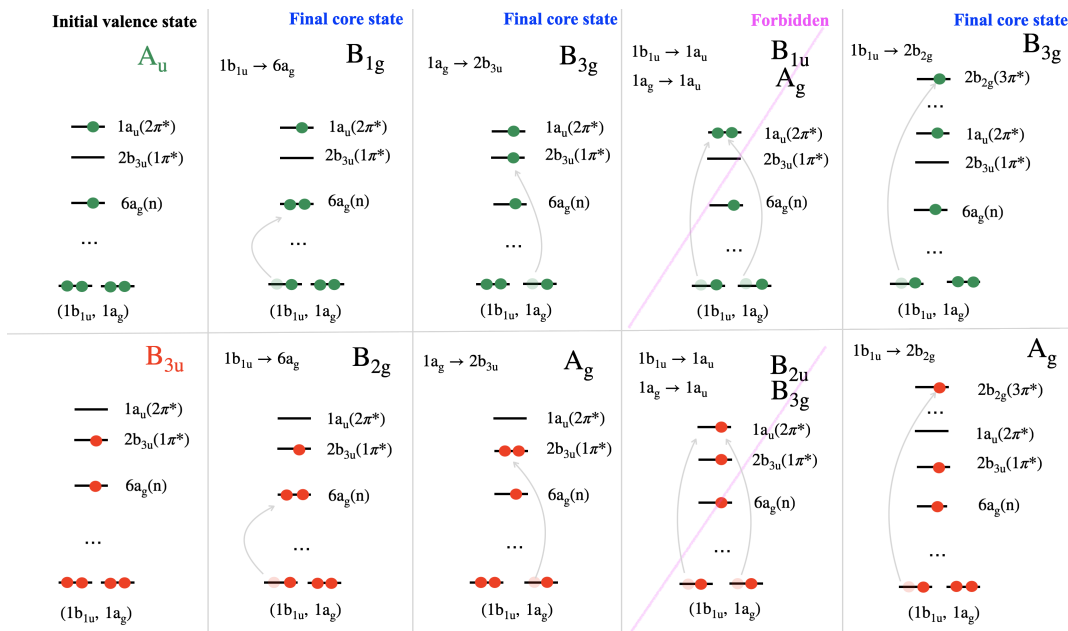


Fig. S8: Schematics of the main (dipole allowed) transitions in the XA spectra of the ${}^1B_{3u}(n\pi^*)$ and ${}^1A_u(n\pi^*)$ states at D_{2h} symmetry at the nitrogen K-edge. As indicated, the core excitations of the two states involve the same orbital transitions, but the final symmetry of the core state is different. From 1A_u , final dipole-allowed core state are B_{1g} , B_{2g} and B_{3g} . From ${}^1B_{3u}$, final dipole-allowed core state are B_{2g} , B_{1g} and A_g . Hence, transitions from the N 1s orbitals to $1a_u(2\pi^*)$ are dipole forbidden in D_{2h} .

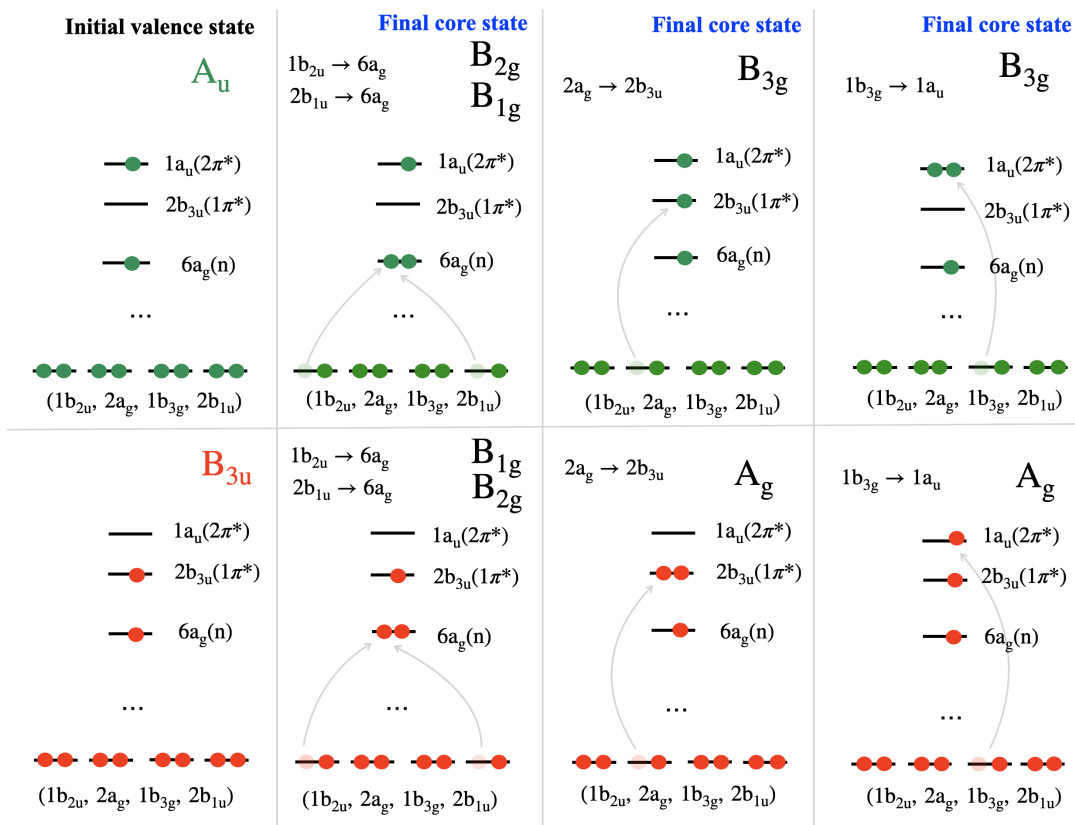


Fig. S9: Schematics of the main transitions in the XA spectra of the $^1B_{3u}(n\pi^*)$ and $^1A_u(n\pi^*)$ states at D_{2h} symmetry at the carbon K-edge. As indicated, the core excitations of the two states involve the same orbital transitions, but the final symmetry of the core state is different. From 1A_u , final dipole-allowed core state are B_{1g} , B_{2g} and B_{3g} . From $^1B_{3u}$, final dipole-allowed core state are B_{2g} , B_{1g} and A_g .

2.2 RASPT2 calculations

RASPT2 calculations of the X-ray absorption spectra (XAS) of valence-excited states of pyrazine in combination with trajectory-based surface hopping (SH) dynamics performed at the ADC(2) level of theory have been used to simulate the time-resolved X-ray absorption spectra (TR-XAS) at the nitrogen K-edge.

Moreover, we also provide an interpretation of the TR-XAS experiments measured at the nitrogen and carbon K-edges for longer time-delays with relaxed geometries of the S_1 state provided by CASPT2 geometry optimization. The influence of the solvent in the spectra is also investigated with a polarizable continuum model (PCM). For calculations at the nitrogen K-edge, we used the Roos Augmented Double Zeta ANO basis set [1] with the contraction [4s3p2d] for N and the ANO-L-DZVP basis set for C and H. For the carbon K-edge calculations, we used the ANO-L-DZVP basis set on all atoms.

Core-excited states were computed by placing the pertinent core orbitals in the RAS1 space and enforcing single electron occupation in it using the HEXS projection technique [2] available in OPENMOLCAS (30), which corresponds to applying the core-valence separation [3]. RAS2 was used for complete electron distribution, i.e., to define the complete active space for the valence electrons while RAS3 was kept empty.

We used the same active space described previously by Northey et al. [4]: the 1s orbitals of interest in the RAS1 subspace (two orbitals in case of N and four orbitals in case of C) and eight valence orbitals and ten electrons in the RAS2 subspace (two n_N lone-pairs, three π and three π^*). Throughout, we will refer to this active space with the short notation RASPT2/RAS2(10e,8o). The active orbitals computed at the Franck–Condon (FC) geometry are schematically represented in Fig. S10.

Dynamical correlation effects are further included in the reference space using the regularized multi-state restricted-active-space perturbation theory of the second-order (RMS-RASPT2) approach [5]. An imaginary level shift of 0.25 Hartree was applied to avoid intruder-state singularities. IPEA shift has not been used. For the nitrogen K-edge calculations, initial valence and final core-excited states were obtained by state averaging over 5 and 15 states, respectively. For the carbon K-edge calculations, we state-averaged the same number of initial and 25 final core-excited states.

The ground-state XA spectra at the carbon and nitrogen K-edges computed at the RASPT2/RAS2(10e,8o) level along with the natural transition orbitals (NTOs) of the main transitions are shown in Fig. S11. The choice of active space containing three π^* orbitals and no σ^* or Rydberg orbitals in the active space means that transitions to the latter orbitals cannot be described at the current level of theory. Therefore, some peaks are missing in the simulated spectrum, but the peaks that are present match very well with the experiment.

The spectra computed with the equilibrium geometry of the ground state (FC) and the equilibrium geometry of the first excited state (S_1), both in vacuum, are shown in Fig. S12. The same but using the PCM to mimic solvent effects on the liquid phase are shown in Fig. S13.

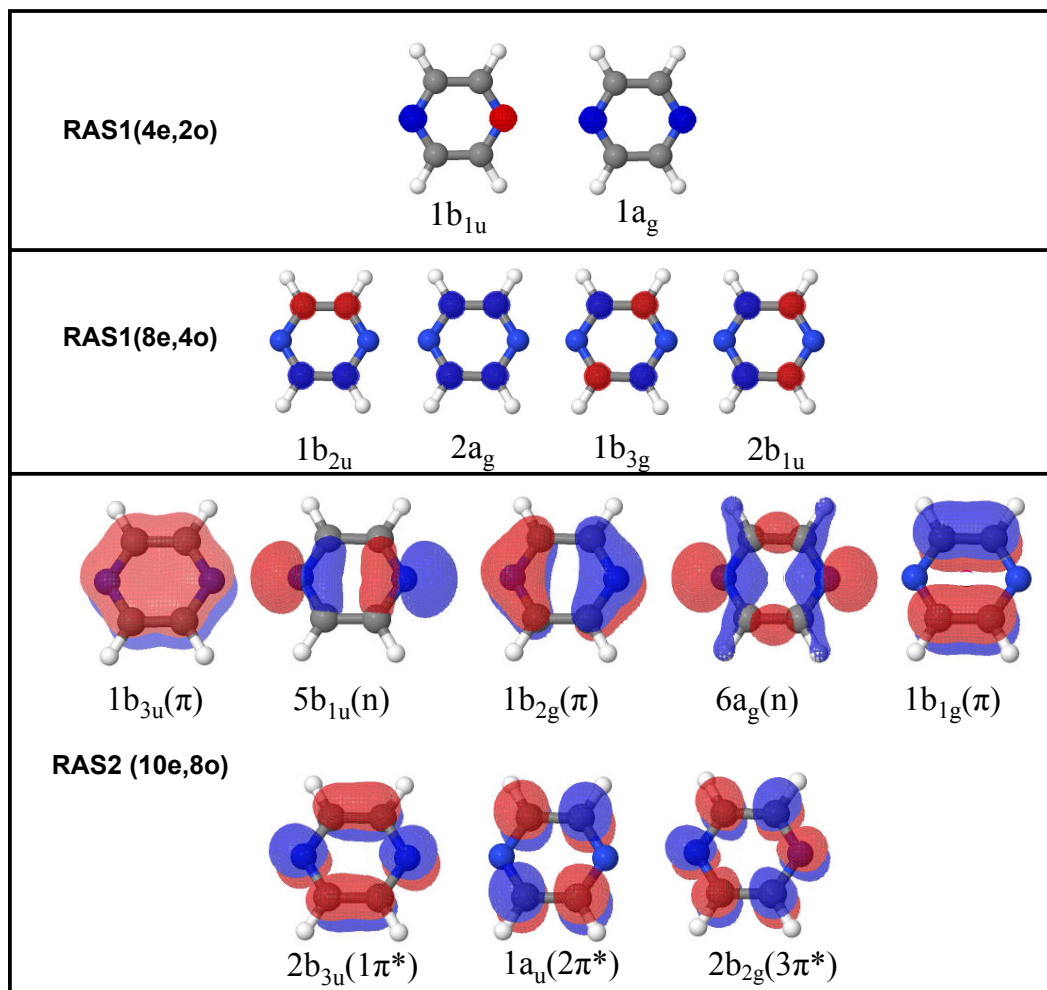


Fig. S10: RASSCF active spaces. RAS1(4e,2o) + RAS2(10e,8o) are used for the nitrogen K-edge calculations, while RAS1(8e,4o) + RAS2(10e,8o) are used for the carbon K-edge calculations.

One advantage of using the RASPT2 approach for TR-XAS is that it can reproduce all orbital configurations, such as $1h1p$, $2h2p$, $3h3p$, etc, within the RAS2 subspace. As long as the selected active space is large enough to account for all important orbital configurations, which is barely guaranteed. On the other hand, the RASPT2 approach has some disadvantages when compared to other single reference methods. It tends to be computationally expensive and time-consuming. Additionally, the accuracy of the calculations strongly relies on the choice of the active space and the number of states included in the state average.

2.3 CCSD and CC3 calculations

Calculations on pyrazine in gas-phase using CCSD and CC3 were performed with the eT program (33, 34). Core-valence separation [6] is employed to obtain core-excited states. To ensure that the valence-excited states are orthogonal to the core-excited

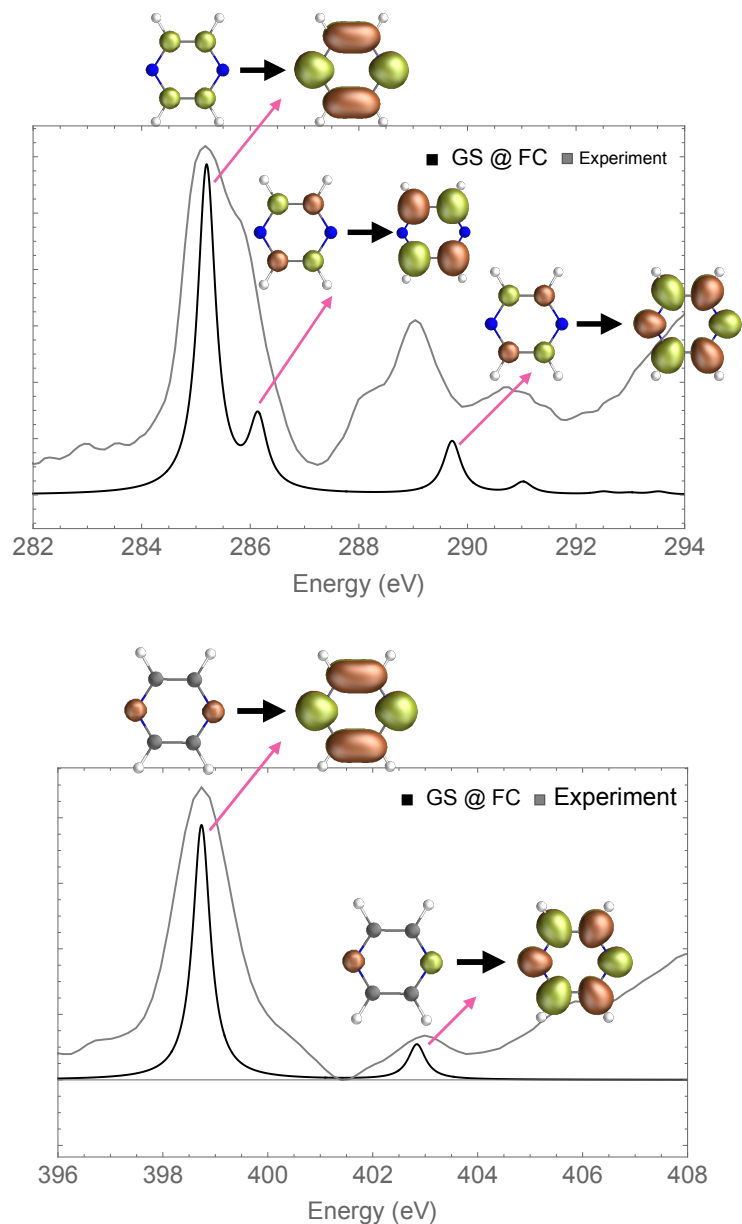


Fig. S11: Ground-state XA spectra (with NTO-based peak-assignments) at the carbon (upper panel) and nitrogen (lower panel) K-edges computed at the RASPT2/RAS2(10e,8o) level versus experiment. Note that no transitions to σ^* are present in the RASPT2 simulated spectra, since these orbitals were not included in the active space.

states the inverse projection (i.e. removing the contributions of core orbitals) is used for the valence excited states.

The X-ray absorption spectrum of the ground state at the carbon and nitrogen K-edges along with the NTOs of the main transitions are shown in Fig. S14. For these calculations, the cc-pVDZ basis set plus additional Rydberg-type functions generated according to Kaufmann, Baumeister, and Jungen's prescription [7] was used. The

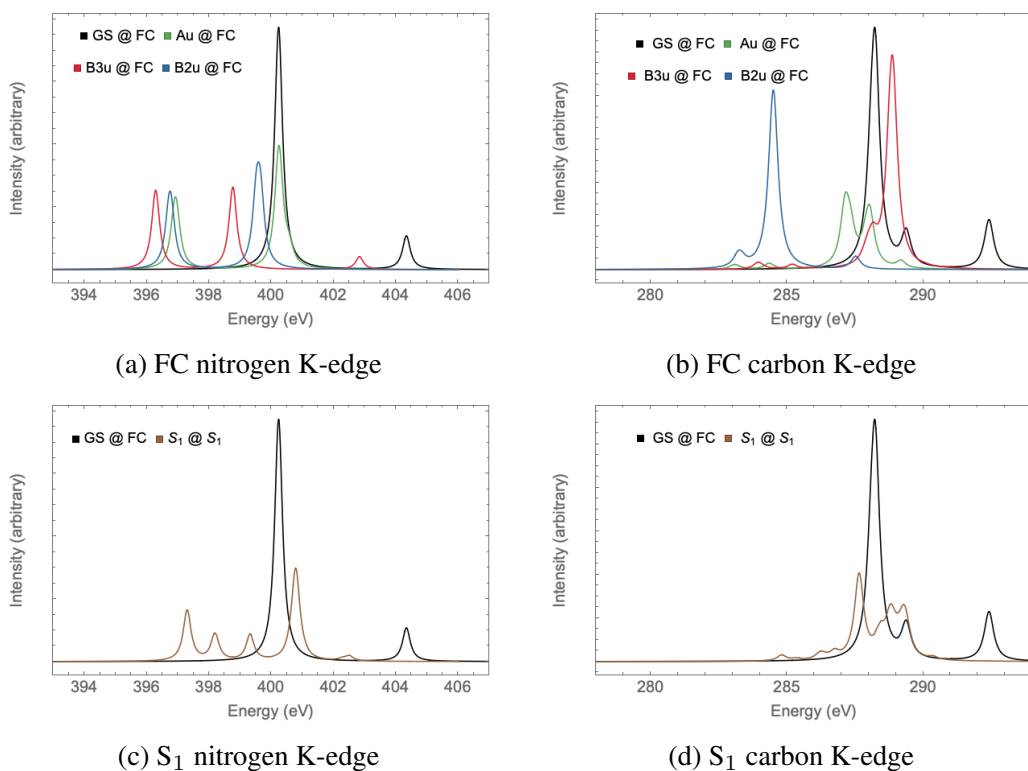


Fig. S12: RASPT2 spectra computed with the equilibrium geometry of the ground state (FC) and the equilibrium geometry of the first excited state (S_1) in vacuum. The S_1 equilibrium geometry was optimized at the CASPT2 level. The computed spectra have been convoluted with Lorentzian functions using $\text{HWHM} = 0.2$ eV. No energy shift has been applied to the calculated energies.

X-ray absorption of the ground and excited states at the Franck-Condon and S_1 minimum geometry was calculated using cc-pVDZ only, and the spectra are depicted in Fig. S15. Additionally, X-ray absorption spectra were calculated for geometries sampled every 10 fs from 34 ADC(2)/aug-cc-pVDZ SH trajectories using the cc-pVDZ basis set. The resulting false color plot is shown in Fig. S26. In the nitrogen spectra, all peaks have been shifted by -2.72 eV to match the ground state bleach. Peaks predicted to lay above the ground state bleach involve significant double excitation character with respect to the ground state and are thus not described as accurately as the pre-edge peaks at the CC3 level. For this reason, coupled cluster calculations using full triples (CCSDT) and the STO-3G basis have been performed using MRCC [8–10] as a benchmark of the CC3 results. Based on these calculations, an additional shift of -2.6 eV was applied to the core excitations from the valence excited states with an excitation energy larger than the ground state bleach.

In the carbon spectra, all peaks have been shifted by -2.6 eV to match the ground state bleach. Based on CCSDT/STO-3G calculations performed with the eT program (33), the excitations from the valence excited states with an excitation energy larger than the ground state bleach have been additionally shifted by -2.0 eV.

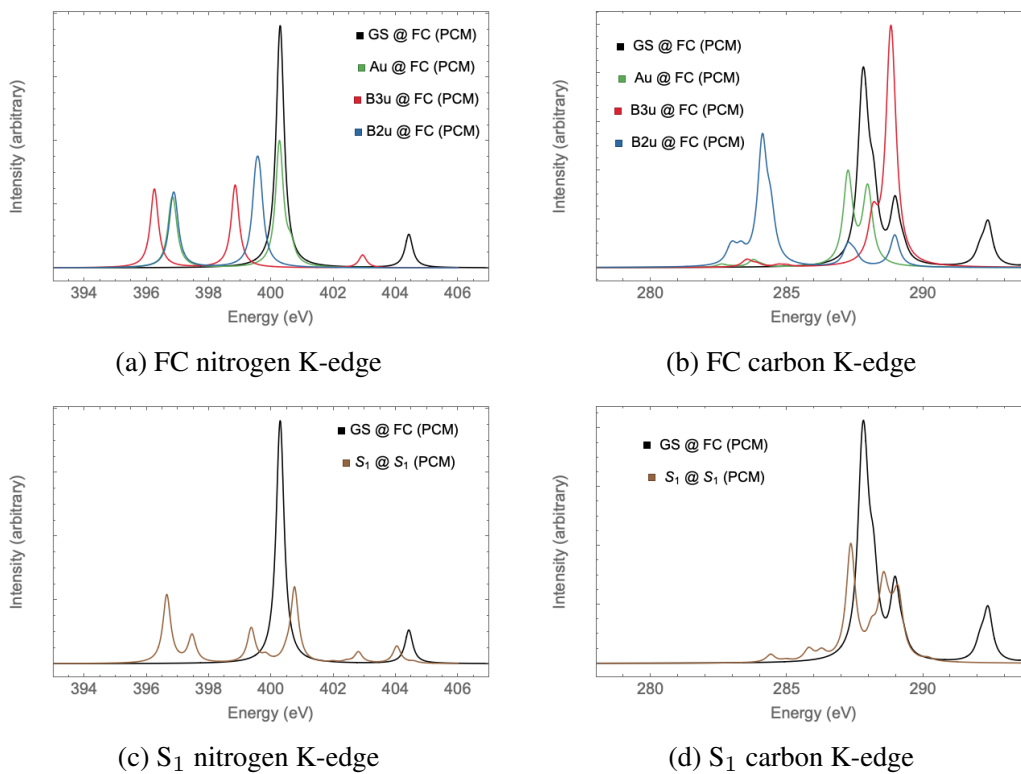


Fig. S13: RASPT2 spectra computed with the equilibrium geometry of the ground state (FC) and the equilibrium geometry of the first excited state (S_1) using a polarizable continuum model (PCM) to mimic solvent effects. The computed spectra have been convoluted with Lorentzian functions using $\text{HWHM} = 0.2$ eV. No energy shift has been applied to the calculated energies.

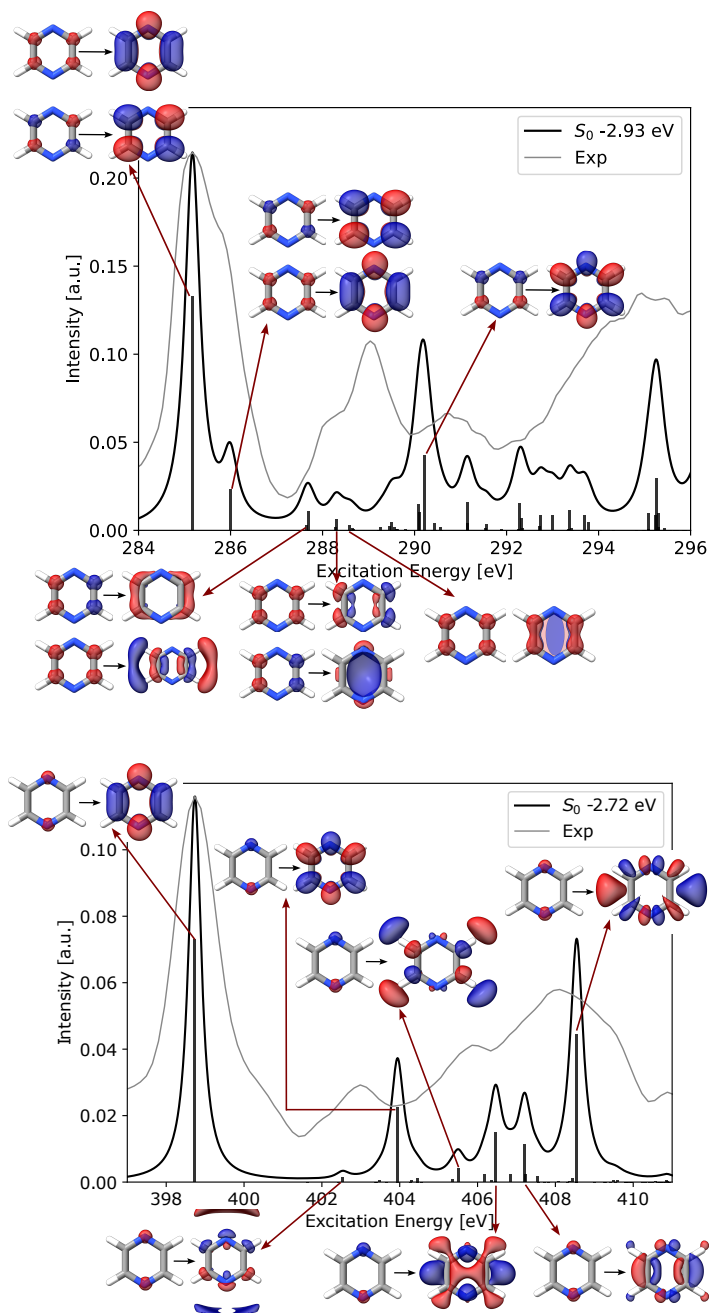


Fig. S14: Ground state XA spectra at the carbon and nitrogen K-edges computed at the CC3 level of theory using the cc-pVDZ basis plus additional Rydberg type functions generated according to Kaufmann, Baumeister and Jungen's prescription [7] with quantum numbers $n = 2, 2.5, 3$ and angular momentum s and p . NTOs of the main transitions are reported for assignment.

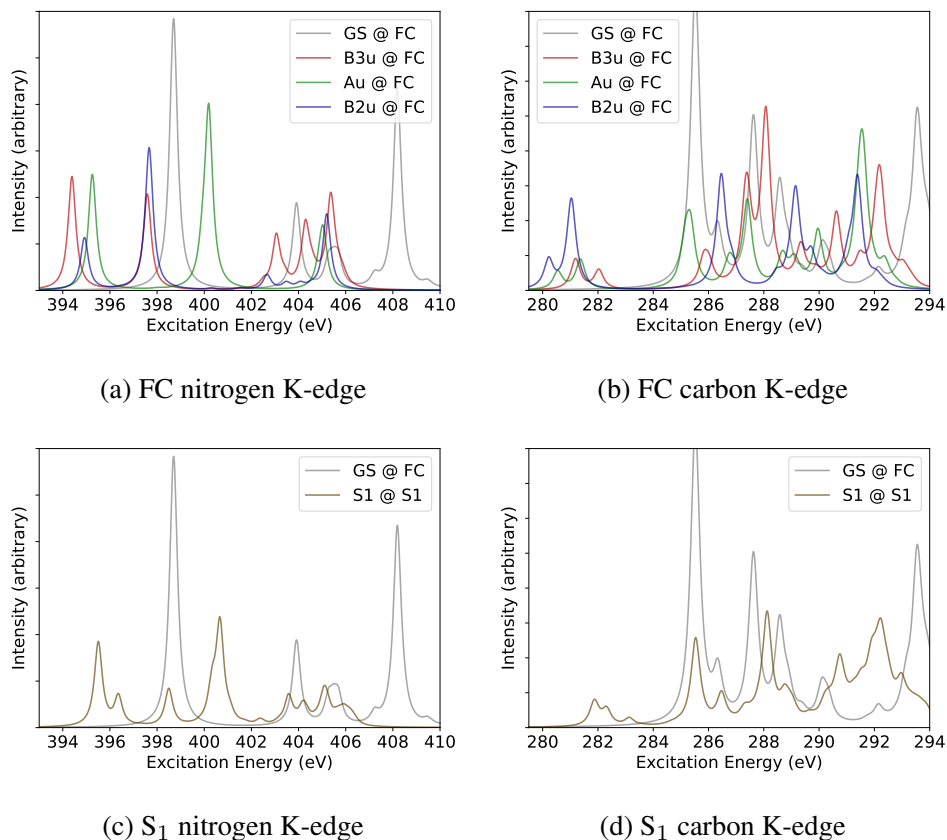


Fig. S15: CC3 spectra computed at the equilibrium geometry of the ground state (FC) and the equilibrium geometry of the first excited state (S_1) in vacuum. The S_1 equilibrium geometry was optimized at the CASPT2 level. The computed spectra have been convoluted with Lorentzian functions using $\text{HWHM} = 0.2 \text{ eV}$.

2.4 Comparison of static CC3 and RASPT2 spectra with experiment at the Carbon and Nitrogen K-edges

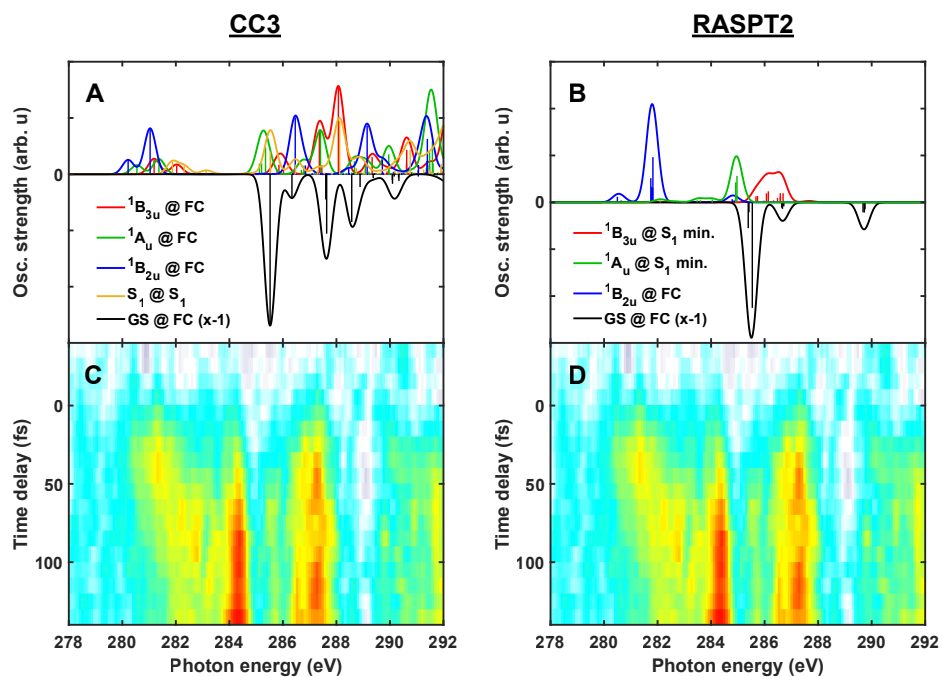


Fig. S16: Carbon K-edge excited-state XA spectra calculated using CC3/cc-pVDZ (A) and RASPT2/RAS2(10e,8o) (B) at both the FC and relaxed geometries for the first valence excited state (S_1). (C,D) Experimental differential absorbance spectra at the carbon K-edge. Note that some transitions are missing in the RASPT2 simulated spectra, since σ^* orbitals were not included in the active space.

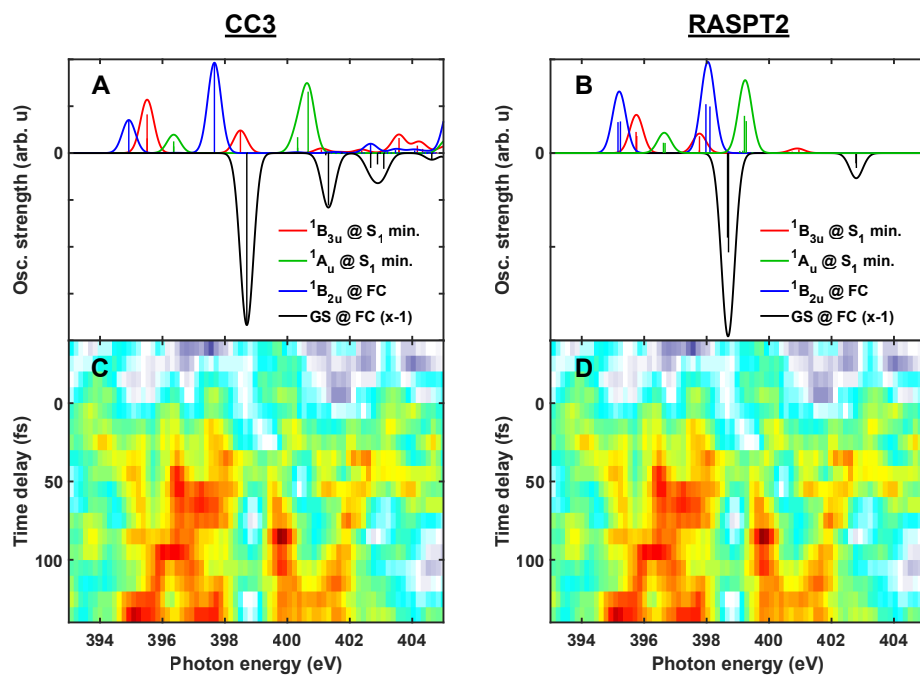


Fig. S17: Nitrogen K-edge excited-state XA spectra calculated using CC3/cc-pVDZ (A) and RASPT2/RAS2(10e,8o) (B) at both the FC and relaxed geometries for the first valence excited state (S_1). (C,D) Experimental differential absorbance spectra at the nitrogen K-edge. Note that some transitions are missing in the RASPT2 simulated spectra, since σ^* orbitals were not included in the active space.

2.5 Nuclear dynamics

2.5.1 Simulated UV spectra

The gas phase and solution UV absorption spectra are shown in Fig. S18a. The spectra are calculated at the ADC(2)/aug-cc-pVDZ level (as implemented in the Turbomole program package [11, 12]) based on an ensemble generated from the harmonic ground state Wigner distribution. For the vacuum spectrum a total of 4000 geometries of pyrazine was sampled. To model the effect of solvation, two water molecules (hydrogen bonded to the nitrogen atoms) were added while the rest of the effect of the environment was modeled implicitly using the conductor like screening model (COSMO) [13, 14]. For this system 2000 initial conditions were sampled from the Wigner distribution with the six lowest frequency normal modes (corresponding to motion of the water molecules relative to pyrazine) frozen as such large amplitude motions are not well described by this approximation.

The first two peaks of the experimental spectrum are reproduced at the ADC(2) level, with a shift of approx. 0.16 eV with respect to the experiment. We see that the solvent shift of the spectrum is correctly reproduced by a combination of two explicit water molecules and COSMO for the bulk environment. Adding either of these effects by itself also resulted in a shift of the spectrum, but by a smaller amount. In Fig. S18b the density of states in the nuclear ensemble is shown, decomposed into contributions from the states of different character. We see that the solvent shifts the two $n\pi^*$ states and the ${}^1B_{2u}(\pi\pi^*)$ state in opposite directions, with the greatest effect on the ${}^1A_u(n\pi^*)$ which is shifted above the ${}^1B_{2u}(\pi\pi^*)$ state at most geometries.

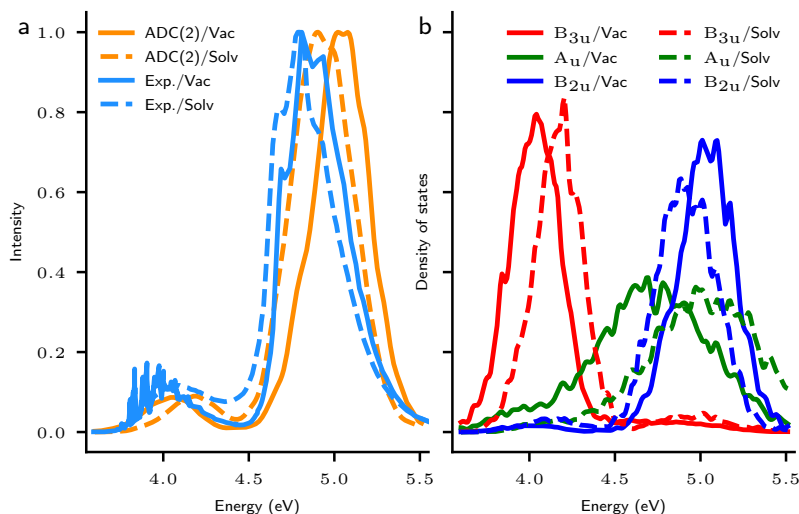


Fig. S18: a) Simulated and experimental UV absorption spectrum of pyrazine in vacuum and in solution. b) Density of states of pyrazine calculated at the ADC(2)/aug-cc-pVDZ level for the ensemble in vacuum and in solution.

2.5.2 Fewest-Switches Surface Hopping calculations

Nonadiabatic dynamics simulations were based on the locally diabatic variant of the fewest-switches surface hopping algorithm (LD-FSSH) with potential energy surfaces (PESs) calculated at the ADC(2)/aug-cc-pVDZ level, following a previous benchmark of the method [15]. This procedure was also successfully used to simulate the time-resolved photoelectron spectrum [16]. A total of 170 initial conditions for nonadiabatic dynamics were randomly (weighted by oscillator strengths) selected from the ground state ensemble among all states falling in an energy window between 4.56 eV and 4.92 eV (excitation window A). This energy window captures the low-energy part of the peak in Fig. S18. Trajectories were propagated for 200 fs using a time step of 0.5 fs. Geometries were sampled from time slices of these trajectories and XA spectra from the currently populated state $L_i(t)$ to a manifold of final core excited states were calculated at the sampled geometries. The TR-XAS spectrum was calculated using the nuclear ensemble approach

$$\sigma(E, t) \propto \sum_i \sum_F \Delta E_{L_i(t)F} |\mu_{L_i(t)F}|^2 k(E - E_{L_i(t)F}, \delta), \quad (1)$$

where the sums are over all trajectories i and final states F , ΔE and μ are the (shifted) energy difference and cross sections between the currently populated state $L_i(t)$ and final state F at geometry $R_i(t)$.

For the solution model, an identical computational procedure was employed as in the gas phase to obtain results which are directly comparable. A total of 187 initial conditions were selected for propagation. Hydrogen transfer from the water molecule to the nitrogen atom of pyrazine occurred in one single trajectory. The population dynamics of the remaining trajectories was similar to the one in vacuum. To test the impact of the excitation window on the dynamics, an additional set of (54 in vacuum, 94 in solution) trajectories was calculated with excitation energies between 4.92 eV and 5.5 eV encompassing the higher energy part of the second peak of the UV spectrum of pyrazine (excitation window B).

Analysis of the trajectories and of the potential energy scans was based on projecting the electronic wave functions $\{|\Phi(\mathbf{R})\rangle\}$ calculated at each geometry onto the wave functions of the ground state minimum geometry $\{|\Phi(\mathbf{R}_0)\rangle\}$. The squares of the elements of an orthogonalized matrix of coefficients obtained in this way [16, 17] are then used as a quantitative measure of the electronic character of each state at each geometry described in terms of ${}^1B_{3u}(n\pi^*)$, ${}^1A_u(n\pi^*)$, ${}^1B_{2u}(\pi\pi^*)$ state contributions. Figure S19 shows the diabatic populations in each set of trajectories. The three sets of trajectories share the same qualitative picture of population dynamics. However, we also see some differences in the population oscillations between the 1A_u and ${}^1B_{3u}$ states depending on the excitation window. This is especially true at very early times where the first maximum of the ${}^1B_{3u}$ population seen at higher energies is missing in the lower excitation window. We also see that the population of the 1A_u is lower in solution than in vacuum.

To support the qualitative description of the dynamics shown in Fig. 4a of the manuscript, we analyze the motion of FSSH trajectories along the 8a and 8b modes in

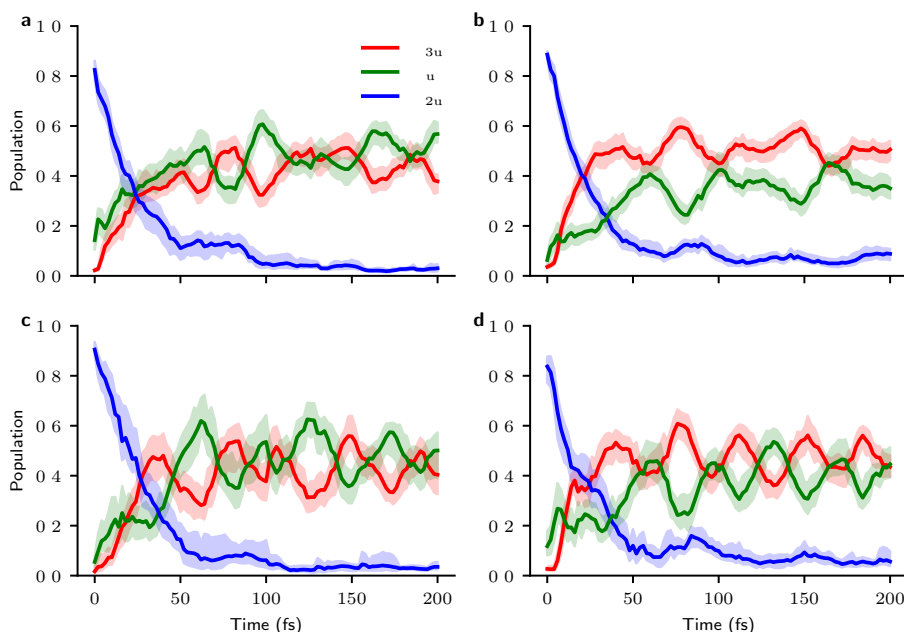


Fig. S19: Diabatic populations along FSSH trajectories of (a, c) pyrazine excited in excitation windows A and B and (b, d) pyrazine in solution excited in excitation windows A and B. Shaded areas represent 95% confidence intervals for the population of each state estimated using the bootstrap method

Fig. S20. The trajectories have been grouped into two sets depending on whether their motion around the CI can primarily be described as clockwise or counterclockwise and the counterclockwise by looking at their motion at each time step with respect to a rolling average representing the central axis at the given time. As expected from symmetry arguments, the number of trajectories falling into each category is approximately the same.

2.5.3 Comparing FSSH and MCTDH calculations

Additional dynamics simulations were performed for the three-state diabatic model Hamiltonian developed by Sala *et al.* [18]. This model includes four electronic states (the ground state and the three lowest excited states) and nine vibrational modes (ν_{6a} , ν_1 , ν_{9a} , ν_{8a} , ν_{10a} , ν_4 , ν_5 , ν_3 , ν_{8b}). The nuclear dynamics for this model systems are propagated using FSSH and also the MCTDH method [19, 20] implemented in the Quantics package [21]. For details on the model system and the MCTDH propagation, the reader is referred to Ref. [18]. Populations obtained for the chosen model using FSSH and MCTDH were previously shown to be in good agreement between methods and also with full dimensional ADC(2) calculations [15]. In Fig. S21 we confirm this agreement and also show that the population oscillations disappear when coupling between the 1A_u and $^1B_{3u}$ states along the Q_{8b} mode is set to zero.

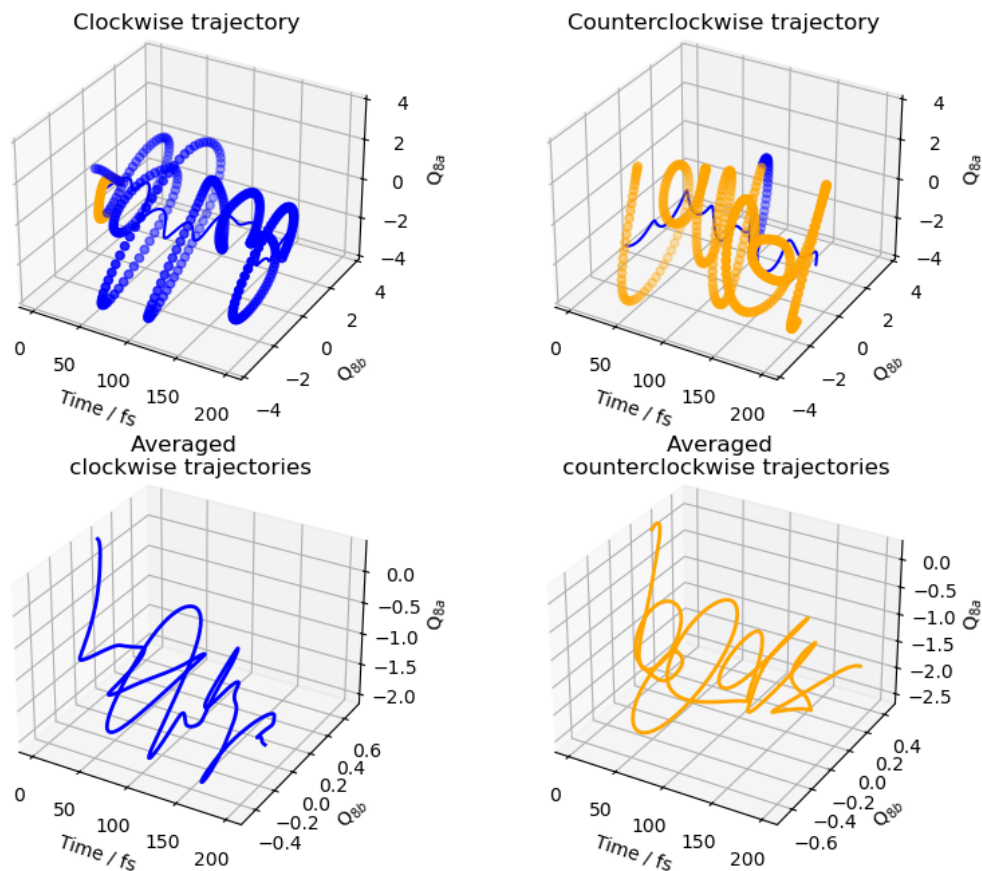


Fig. S20: Dynamics of the FSSH trajectories along the 8a and 8b modes over time. The upper panels show an example trajectory moving primarily clockwise (blue) and counterclockwise (orange) around an average (blue full line). The lower panels show the average dynamics of all trajectories in each group.

In Fig. S22, we show the 2D diabatic reduced density of the wave packet along the 8a and 8b modes. Upon passing through the CI, amplitude is equally sent towards both sides around $Q_{8b} = 0$ on the 1A_u state. This coincides with a reflection along the 8a mode sending the system back towards the CI. The two components of the wave packet then recombine on the $^1B_{3u}$ surface on the other side of the CI and the process is repeated. Before 100 fs, a recurrence of the $^1B_{2u}$ state occurs after which the wave packet is spread out further, but oscillations along the 8a mode along with the spreading + recombining of the wave packet along the 8b mode are still visible.

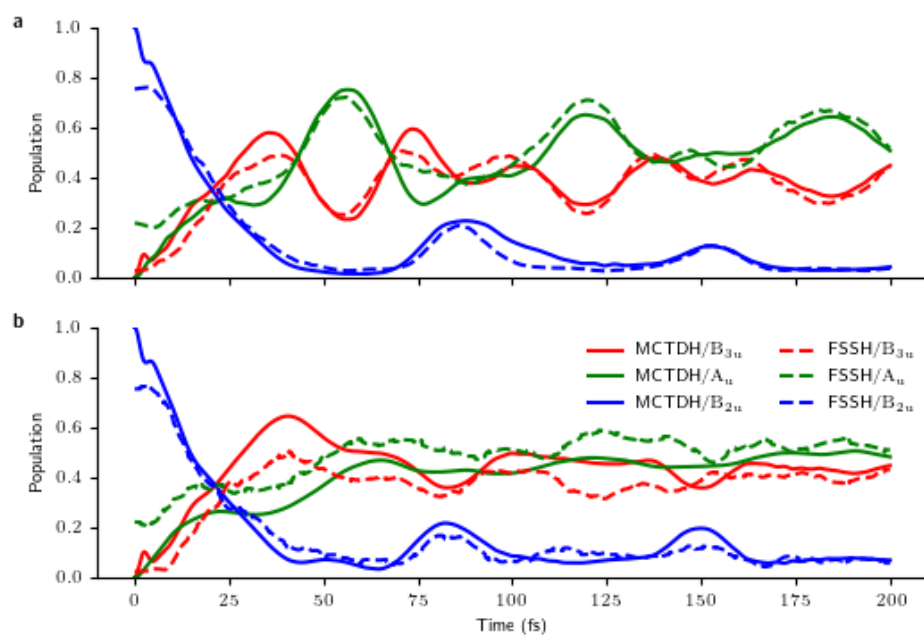


Fig. S21: Comparison of diabatic populations from MCTDH and FSSH calculations performed using (a) the full three-state model from Ref. [18] and (b) the same model, but with coupling between the $1A_u$ and $1B_{3u}$ states along the 8b mode set to zero.

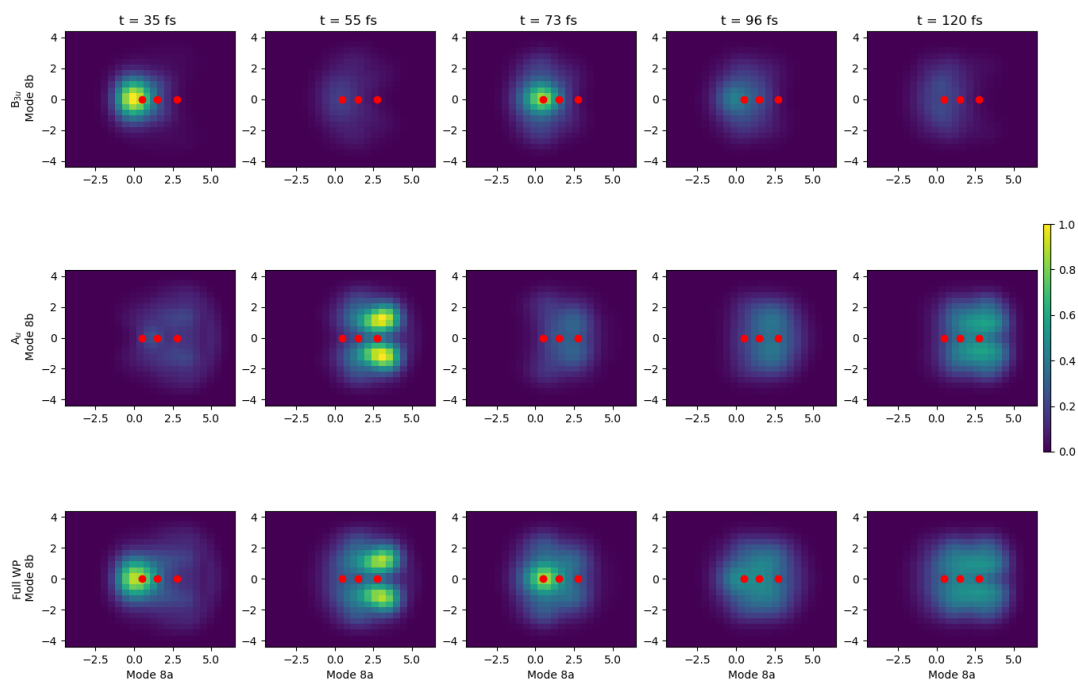


Fig. S22: Motion of the wave packet in the space spanned by the 8a and 8b modes on the potential-energy surfaces from Ref. [18]. Components of the wave packet on the ${}^1B_{3u}$ (top row) and 1A_u (middle row) and the two components together (bottom row) are shown. The red dots mark the positions of the ${}^1B_{3u}$ minimum, the CI and the 1A_u minimum (from left to right).

2.6 Simulated TR-XAS

Carbon and nitrogen K-edge TR-XAS up to 200 fs were calculated at the RASPT2/RAS2(10e,8o) levels of theory based on time slices taken every 2 fs from 34 of the gas phase trajectories.

Calculating the spectra in this way introduces a discontinuity when sampling geometries from trajectories where the currently populated state is, obviously, calculated at the ADC(2)/aug-cc-pVDZ level and now needs to be re-calculated at a different level of theory. To ensure the consistency of the calculated results, we checked the distribution of excitation energies for all geometries sampled from the dynamics calculated at the ADC(2)/aug-cc-pVDZ, CC3/cc-pVDZ and RASPT2/RAS2(10e,8o) levels of theory.

The overall agreement between the three methods is very good, with only a slight difference in the distribution of energies of the S_2 state at the RASPT2 level. However, taking only the subset of geometries at $t = 0$ we see that the agreement between RASPT2 and the other methods is significantly worse, with a significant shift of the S_2 state which is the initially populated state in many trajectories. Despite this difference in the region of the ground state minimum, the energies become much closer at later times, indicating that the shapes of the PES are similar at all three levels. To fix the issue with the different ordering of the states at some geometries at early times, we apply a reordering based on the overlap of the excited state wave functions at the ADC(2) and RASPT2 levels. For the simulated XAS we always choose the RASPT2 state with the largest overlap with the ADC(2) excited state that is populated at the given geometry during the dynamics simulations.

Fig. S23a shows the simulated spectrum at the RASPT2/RAS2(10e,8o) level. The positions of the peaks are accurately represented by the simulated spectrum. Interaction between the two $n\pi^*$ states is clearly visible from the oscillations in the intensity of the peaks. However, these oscillations still have a significantly different time scale and amplitude to the ones seen in the experiment.

As with the nitrogen K-edge, we see a good qualitative agreement with the experimental spectrum. The main difference is the shift of the peaks just below and above the edge in opposite directions, bringing them significantly closer to each other than they are in the experiment.

Fig. S24 shows the integrated intensities of the peaks in the simulated spectra. We see the oscillations and relative intensities of the peaks. These lineouts are highly correlated, but not directly proportional, with the populations of the diabatic states to which the peaks are assigned.

The nitrogen K-edge TR-XAS was also simulated at the CC3/cc-pVDZ level using time slices taken every 10 fs from the same trajectories used for the RASPT2/RAS2(10e,8o) spectra and the same procedure for handling the discontinuity between electronic structure methods for dynamics and spectrum simulations. The state ordering between the ADC(2) and CC3 calculations is significantly more consistent, even at early times close to the CI, than when comparing with RASPT2 calculations.

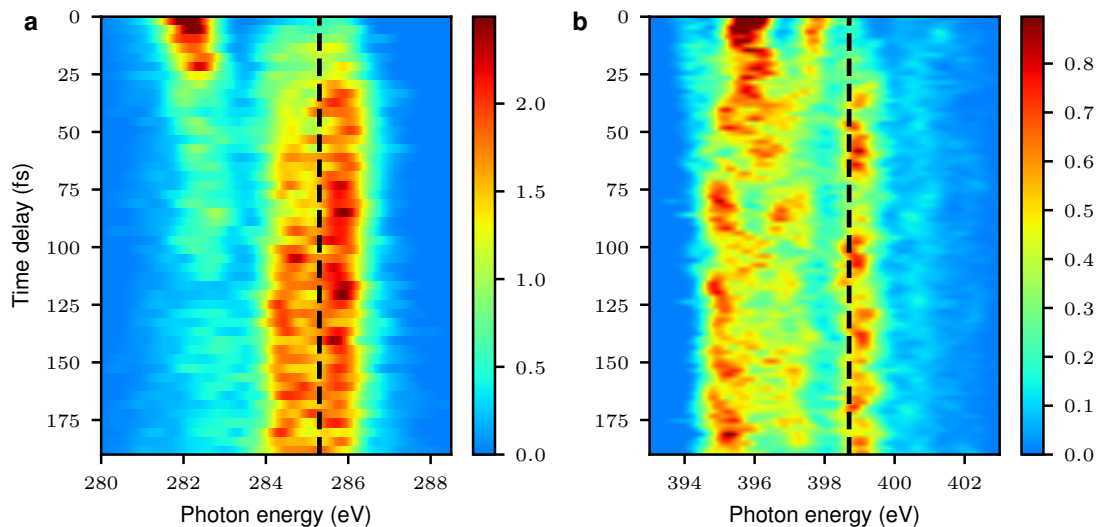


Fig. S23: (a) Carbon and (b) nitrogen K-edge excited-state XA spectra calculated at the RMS-RASPT2/RAS2(10e,8o) level based on 34 FSSH trajectories calculated at the ADC(2)/aug-cc-pVDZ level. The simulated spectrum has been shifted by -2.9 eV (carbon K-edge) and -1.5 eV (nitrogen K-edge). The position of the ground state bleach is marked by the dashed black line.

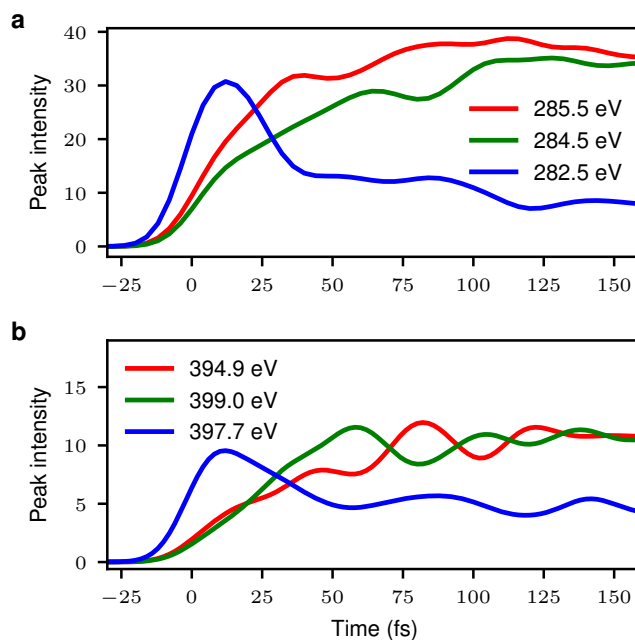


Fig. S24: Integrated intensities of selected peaks in the simulated (a) carbon K-edge and (b) nitrogen K-edge XA spectra calculated at the RMS-RASPT2/RAS2(10e,8o) level. The red, green and blue lines represent peaks primarily originating from the ${}^1B_{3u}(n\pi^*)$, ${}^1A_u(n\pi^*)$ and ${}^1B_{2u}(\pi\pi^*)$ states, respectively. The full spectrum is shown in Fig. S23.

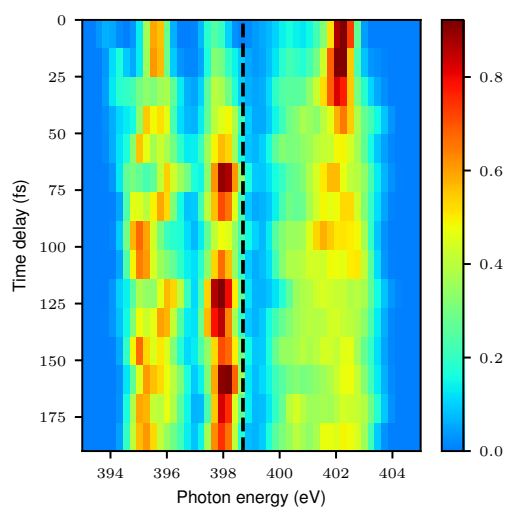


Fig. S25: Nitrogen K-edge excited-state XAS spectra calculated at the CC3/cc-pVDZ level based on 34 FSSH trajectories calculated at the ADC(2)/aug-cc-pVDZ level. The position of the ground state bleach is marked by the dashed black line. The simulated spectrum has been shifted by -2.75 eV with an additional -2.6 eV shift for the above-edge peaks (see Sec 2.3).

3 Interpretation of the solvent effects

3.1 Concentration-dependent absorption spectra

Fig. S26 shows the 266 nm UV pump absorbance of pyrazine solutions across a broad range of concentrations, namely ranging from a 1 mM to 5 M. This was achieved by using various liquid jet thicknesses, down to the sub- μm range [22–24], in order to cover the entire dynamic range. The linear increase in absorbance with pyrazine concentration indicates that self-association does not play a major role on the absorption properties of pyrazine at the studied concentrations. The $\sim 18\text{-}\mu\text{m}$ nozzle orifice size, which was used for 1-5 M linear absorption measurements, was utilized for the time-resolved experiments. The 266 nm source was the same as the one used for the time-resolved experiments.

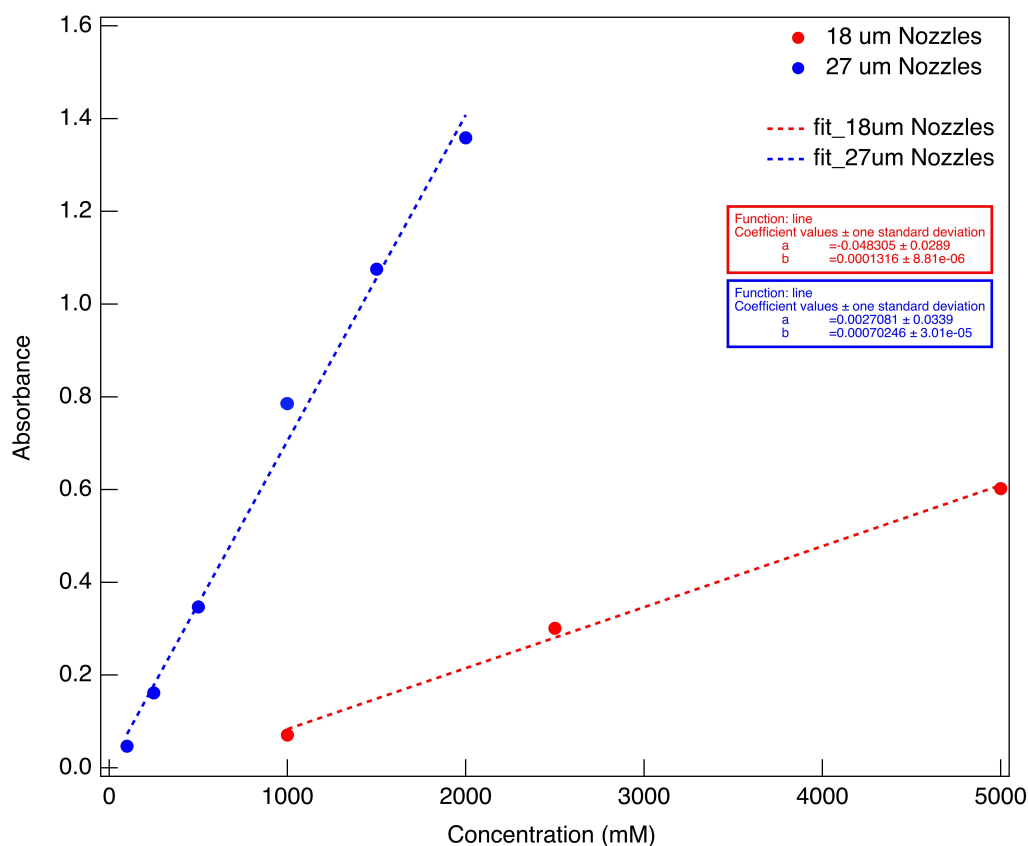


Fig. S26: Absorbance at the pump wavelength (266 nm) by liquid flat jets with different inner diameters of nozzles running aqueous solutions of pyrazine at various concentrations. The linear relationship across the entire concentration range indicates that self-association does not play a major role in the absorption properties of pyrazine at the studied concentrations. The parameters a and b of the linear regressions stand for the intercept and slope, respectively.

Using a standard UV-Vis instrument (Thermo Scientific GENESYS 50), and pyrazine

concentrations in the 0.1-2.5 mM range, the extinction coefficient of aqueous pyrazine solutions was found to be $\epsilon = 10580 \text{ L mol}^{-1} \text{ cm}^{-1}$. Using the jet thickness previously measured for $\sim 27 \mu\text{m}$ nozzle orifice jets [22], the aqueous pyrazine extinction coefficient for jet measurements with these nozzles was extracted via the Beer-Lambert relation and found to be $\epsilon_{27} = 8570 \text{ L mol}^{-1} \text{ cm}^{-1}$, demonstrating reasonable agreement with the value measured from a traditional UV-Vis system. This agreement further suggests that there are no major self-association effects on the absorption properties of aqueous pyrazine even at concentrations above 1 M.

3.2 Self-association effect

The experimental results shown in the previous subsection indicated no major effects of self-association on the UV absorption spectra.

A previous study [25] reported small deviations from the Beer-Lambert law over a very broad range (5.5 orders of magnitude) of concentration.

In this section, we computationally explored whether insight into self-association of the pyrazine molecules

could be obtained from calculations of the UV excitation energies and oscillator strengths of a pyrazine dimer. To this end, we assumed a dimer with a sandwich configuration, where the intermolecular interaction should be the largest, and optimized the geometry at the B3LYP-D3/aug-cc-pVDZ level as in Table S1 and Fig. S27. The optimization yielded as most stable structure a cross-displaced π - π stacked structure, consistent with the CCSD(T) results in Ref. [26]. We then calculated the excitation energies of the dimer at the optimized geometry at the ADC(2)/aug-cc-pVDZ level of theory.

Table S1: Geometry of pyrazine dimer optimized at the B3LYP-D3/aug-cc-pVDZ level of theory; xyz format, coordinates in Angstrom (\AA).

C	2.127257	1.134516	-0.323795
C	1.409320	1.133535	0.877978
C	2.127895	-1.133551	-0.325302
C	1.409930	-1.134621	0.876444
H	2.408516	2.074124	-0.803604
H	1.111302	2.071613	1.349250
H	2.409713	-2.072344	-0.806377
H	1.112321	-2.073489	1.346403
N	2.493008	0.001000	-0.933839
N	1.048120	-0.001038	1.487955
C	-2.334762	0.698987	0.706912
C	-2.333932	-0.701496	0.705570
C	-1.201511	0.700790	-1.257781
C	-1.200694	-0.698182	-1.259106
H	-2.799606	1.254518	1.523908
H	-2.798103	-1.259158	1.521499
H	-0.727873	1.258310	-2.067611
H	-0.726384	-1.253564	-2.070013
N	-1.772184	1.409789	-0.275635
N	-1.770503	-1.409732	-0.278336

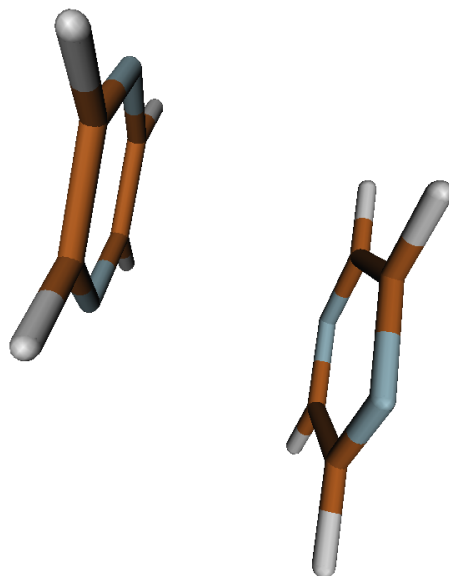


Fig. S27: Visualized geometry of the pyrazine dimer optimized at the B3LYP-D3/aug-cc-pVDZ level.

The energies and oscillator strengths of the excitations of each pyrazine monomer in the dimer and of the dimer as a whole are given in Table S2. NTOs of the dimer excitations are shown in Figure S28.

Table S2: Excited states of each pyrazine monomer in the B3LYP-D3 optimized dimer and of the dimer as a whole, calculated using ADC(2) in conjunction with the aug-cc-pVDZ basis set.

State	Monomer 1 / Monomer 2		Dimer	
	Exc. energy (eV)	Osc. strength	Exc. energy (eV)	Osc. strength
${}^1B_{3u}(n\pi^*)$	4.18153	0.00606	4.16614	0.01371
	4.18085	0.00606	4.17088	0.00153
${}^1A_u(n\pi^*)$	4.78947	0.00000	4.75575	0.00000
	4.78909	0.00000	4.77360	0.00000
${}^1B_{2u}(\pi\pi^*)$	5.20376	0.09022	5.17327	0.06597
	5.20554	0.09024	5.17526	0.06249

In the dimer, the ${}^1B_{3u}(n\pi^*)$ and ${}^1A_u(n\pi^*)$ and ${}^1B_{2u}(\pi\pi^*)$ pairs of states experience a slight red shift from those of the monomers, although by less than 0.1 eV. While the pair of ${}^1A_u(n\pi^*)$ states remains dark, the oscillator strengths of the two ${}^1B_{3u}(n\pi^*)$ states sum up to a value that is slightly larger than twice the strength of the monomer (hyperchromism).

For the ${}^1B_{2u}(\pi\pi^*)$ state, on the other hand, the oscillator strength in the dimer is lower than twice that of the monomer (hypochromism). These results are consistent with the experimental observations.



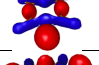
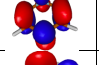
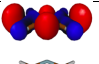

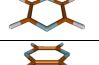
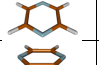
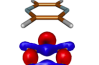
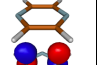
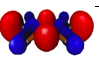
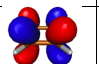


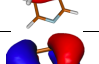
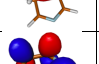
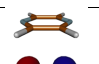
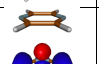
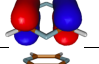
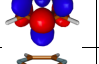
	Energy (eV)	Osc. Str.	Hole	Particle	Weight
State 1	4.166138	0.013710			0.69
					0.16
State 2	4.170876	0.001529			0.69
					0.16
State 3	4.755755	0.000000			0.83
State 4	4.773597	0.000000			0.83
State 5	5.173270	0.065965			0.70
					0.12
State 6	5.175263	0.062492			0.70
					0.12

Fig. S28: Natural transition orbitals of the first 6 valence excited states of pyrazine dimer. ADC(2)/aug-cc-pVDZ results.

3.3 Solvent effects in each excited state

In this section, we study the effects of solvation on pyrazine by building on the spectral simulations based on microsolvation models from Ref. 27. In Ref. 27, 100 snapshots based on an ab initio molecular dynamics (AIMD) simulation for a system where a pyrazine molecule was dissolved in 112 water molecules were obtained. This system corresponds to 0.5 M pyrazine aqueous solution. In each snapshot, the pyrazine molecule and the water molecules in the first and second solvation shells were extracted. The number of extracted water molecules was 24 on average, and the microsolvation model consisting of one pyrazine molecule and 24 water molecules

may qualitatively describe the solvent effects in the present 5M pyrazine aqueous solution, where the unit cell contains one pyrazine and 12 water molecules. For each snapshot of the microsolvation model consisting of the extracted pyrazine and water molecules, the valence excitation energies were calculated at the ADC(2) level, adopting the aug-cc-pVTZ and aug-cc-pVDZ basis sets to the pyrazine and water molecules, respectively. The oscillator strengths for the 100 snapshots were collected and plotted in histogram style in Fig. 5(f) of Ref. 27. Such UV-Vis spectral simulation based on 200 AIMD snapshots was also conducted for an isolated pyrazine molecule and the result was plotted in Fig. 4(a) of Ref. 27.

For one of the 100 snapshots, where the NTOs of the transitions from the ground state to the three lowest adiabatic excited states (\tilde{A} , \tilde{B} and \tilde{C}) were similar to those at the equilibrium geometry of pyrazine, the solvent effects from the water molecules in the first and second solvation shells were investigated by comparing the excitation energies, the oscillator strengths, and the NTOs for the three models: (i) only the pyrazine molecule, (ii) the pyrazine molecule with the water molecules in the first solvation shell, and (iii) the pyrazine molecule with the water molecules in the first and second solvation shells. The excitation energies and the oscillator strengths were given in the “no-COSMO” columns of Table 3 of Ref. 27. The NTOs were given in Table 4 of Ref. 27. As shown in Table 4 of Ref. 27, without water molecules, \tilde{A} , \tilde{B} and \tilde{C} states had almost the pure configuration characters of ${}^1B_{3u}(n\pi^*)$, ${}^1A_u(n\pi^*)$ and ${}^1B_{2u}(\pi\pi^*)$, respectively. Energy ordering of the configuration characters of ${}^1A_u(n\pi^*)$ and ${}^1B_{2u}(\pi\pi^*)$ switched when the water molecules in the second solvation shell were added. Considering the configuration characters in Table 4 of Ref. 27 and the excitation energies given in Table 3 of Ref. 27, it is estimated that the diabatic ${}^1B_{3u}(n\pi^*)$ and ${}^1A_u(n\pi^*)$ states are raised by 0.3 and 0.5 eV, respectively, whereas the diabatic ${}^1B_{2u}(\pi\pi^*)$ state is lowered by 0.2 eV, due to the solute-solvent interactions.

The second absorption band in Fig. 4(a) and Fig. 5(f) of Ref. 27 are separated for the adiabatic \tilde{B} and \tilde{C} states and shown in panels (a) and (b) of Fig. S29, respectively. The dashed bar corresponds to the central wavelength of the pump pulse of the present experiment, considering the difference between the band maximum of the simulated and experimental spectra shown in Fig. 4(a) of Ref. 27. Since the adiabatic \tilde{B} state has the configuration character of ${}^1A_u(n\pi^*)$ at the equilibrium geometry and the excitation from the ground state is dipole forbidden there, contribution from the \tilde{B} state to the second absorption band in the UV-Vis absorption spectrum of pyrazine in the gas phase is minor, as seen in panel (a) of Fig. S29. Meanwhile as seen in panel (b) of Fig. S29, contributions from the \tilde{B} and \tilde{C} states to the second absorption band in the UV-Vis spectrum simulated for the microsolvation model are comparable. The two contributions are almost in equal amount, especially at the energy corresponding to the central wavelength of the experimental pump laser. This behavior is consistent with the switching of the energy ordering observed in Table 4 of Ref. 27 and indicates that a conical intersection between the diabatic ${}^1A_u(n\pi^*)$ and ${}^1B_{2u}(\pi\pi^*)$ states lies in the FC region.

Normalized frequency distribution of the oscillator strength in the energy window of 4.9–5.1 eV of Fig. S29 (a) and (b) are plotted in Fig. S30 (a) and (b), respectively, to examine whether the ${}^1A_u(n\pi^*)$ and ${}^1B_{2u}(\pi\pi^*)$ configurations are

noticeably mixed in the FC region. When the target state has the pure ${}^1A_u(n\pi^*)$ or ${}^1B_{2u}(\pi\pi^*)$ configuration character, the oscillator strength of the transition from the ground state is 0.00 and 0.10, respectively, at the ADC(2)/aug-cc-pVTZ level. Panel (a) thus indicates that the two configurations are not mixed when a pyrazine molecule is isolated. Meanwhile, panel (b) exhibits evidence of the configuration mixing in the FC region by distribution of the oscillator strength around 0.04 due to the solute-solvent interactions. This configuration mixing may enable faster nonadiabatic transition to ${}^1A_u(n\pi^*)$ or almost direct optical transition with the pump laser to the diabatic ${}^1A_u(n\pi^*)$ state when pyrazine is dissolved in water. This interpretation is consistent with the early appearance of the core-excitation peaks which are assigned to the ${}^1A_u(n\pi^*)$ state in the solution phase (see Figs. 2 and 3 of the main manuscript and Fig. S1 of this SI).

The solvent effects observed in the simulation of Ref. 27 also gives possible interpretation of suppression of the oscillatory flow of population between the ${}^1B_{3u}(n\pi^*)$ and ${}^1A_u(n\pi^*)$ states. The potential energy surface of ${}^1A_u(n\pi^*)$ is raised by 0.5 eV whereas that of ${}^1B_{3u}(n\pi^*)$ is raised by only 0.3 eV in the solution phase (compare \tilde{A} - \tilde{B} of bare/no-COSMO and \tilde{A} - \tilde{C} of +second shell/no-COSMO in Table 3 of Ref. 27). The higher the ${}^1A_u(n\pi^*)$ state surface with respect to the ${}^1B_{3u}(n\pi^*)$ state surface, the smaller the area of the ${}^1B_{3u}(n\pi^*)/{}^1A_u(n\pi^*)$ conical intersection becomes. Moreover, energy dissipates from the nuclear wave packet of pyrazine dissolved into the water bath. As a result, the transitions between the ${}^1B_{3u}(n\pi^*)$ and ${}^1A_u(n\pi^*)$ states might be prevented, especially in the direction from ${}^1B_{3u}(n\pi^*)$ to ${}^1A_u(n\pi^*)$.

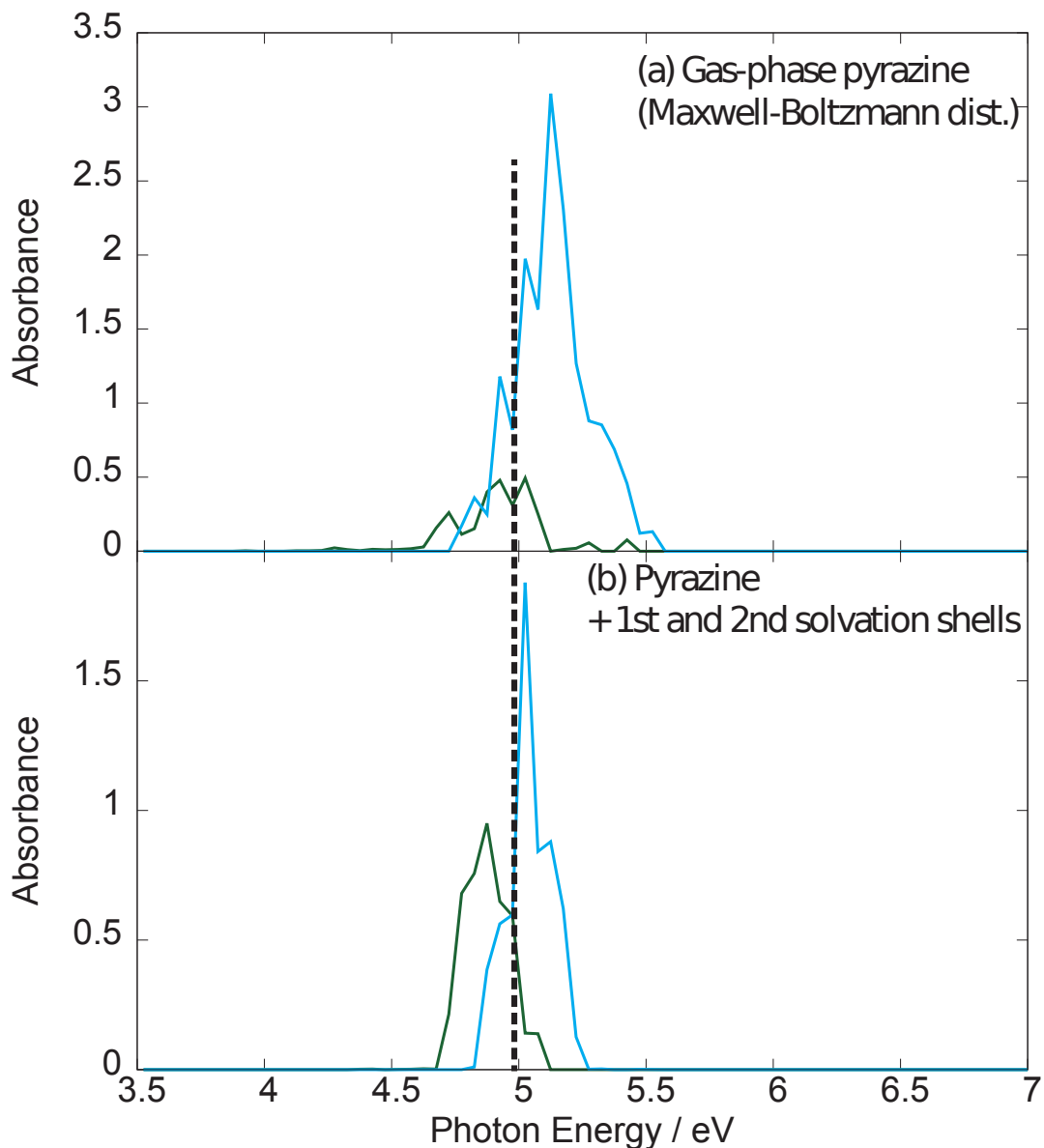


Fig. S29: Absorbances of the electronic transitions from the ground state to the (deep green) \tilde{B} and (cyan) \tilde{C} adiabatic states plotted based on the Maxwell-Boltzmann distributions for (a) pyrazine in the gas phase and (b) pyrazine embedded in the first and second solvation shells of water molecules. The excitation energies were calculated with ADC(2) adopting the aug-cc-pVTZ and aug-cc-pVDZ basis sets to the pyrazine and water molecules, respectively. The dashed bar indicates the energy corresponding to the central wavelength of the pump pulse ($4.66 + 0.31$ eV). These plots are based on computational data for Fig. 4(a) and Fig. 5(f) of Ref. 27.

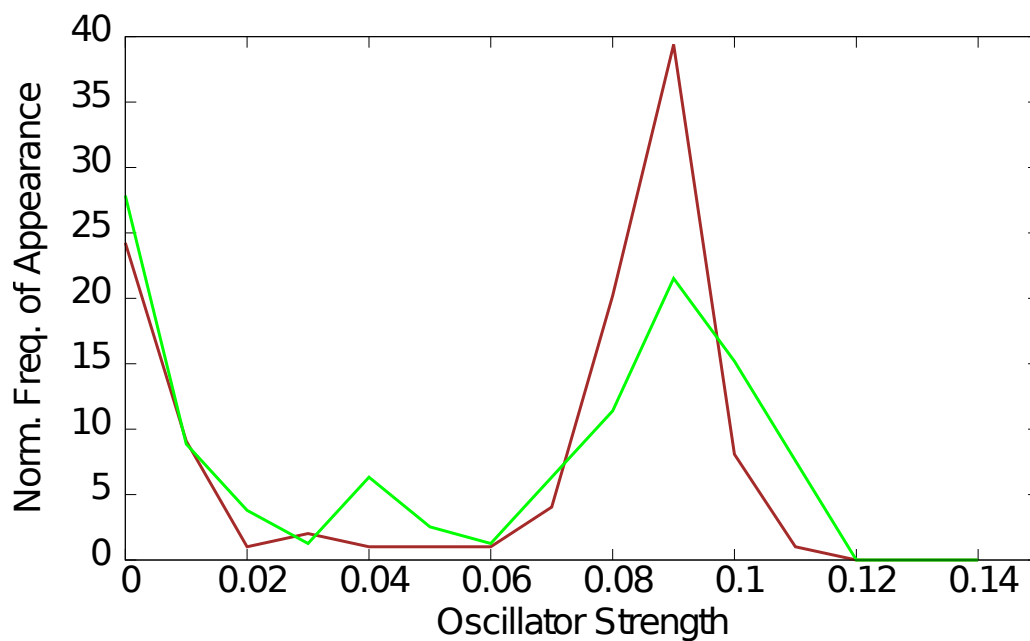


Fig. S30: Normalized frequency distribution of the oscillator strengths in excitation energy of 4.9-5.1 eV calculated for pyrazine (brown) in the gas phase and (green) embedded in the first and second solvation shells of water molecules. The oscillator strengths of the transitions from the ground state to the second and third excited states at the optimized geometry are 0.00 and 0.10, respectively. These plots are based on computational data from Fig. 4(a) and Fig. 5(f) of Ref. 27.

References

- [1] Widmark, P.-O., Malmqvist, P.-Å., Roos, B.O.: Density matrix averaged atomic natural orbital (ANO) basis sets for correlated molecular wave functions. *Theoretica Chimica Acta* **77**(5), 291–306 (1990) <https://doi.org/10.1007/BF01120130>
- [2] Delcey, M.G., Sørensen, L.K., Vacher, M., Couto, R.C., Lundberg, M.: Efficient calculations of a large number of highly excited states for multiconfigurational wavefunctions. *J. Comput. Chem.* **40**(19), 1789–1799 (2019) <https://doi.org/10.1002/jcc.25832>
- [3] Cederbaum, L.S., Domcke, W., Schirmer, J.: Many-body theory of core holes. *Phys. Rev. A* **22**, 206–222 (1980)
- [4] Northey, T., Norell, J., Fouda, A.E.A., Besley, N.A., Odellius, M., Penfold, T.J.: Ultrafast nonadiabatic dynamics probed by nitrogen K-edge absorption spectroscopy. *Phys. Chem. Chem. Phys.* **22**, 2667–2676 (2020) <https://doi.org/10.1039/C9CP03019K>
- [5] Battaglia, S., Fransén, L., Fdez. Galván, I., Lindh, R.: Regularized CASPT2: an Intruder-State-Free Approach. *J. Chem. Theory Comput.* **18**(8), 4814–4825 (2022)
- [6] Coriani, S., Koch, H.: Communication: X-ray absorption spectra and core-ionization potentials within a core-valence separated coupled cluster framework. *J. Chem. Phys.* **143**(18), 181103 (2015) <https://doi.org/10.1063/1.4935712>
- [7] Kaufmann, K., Baumeister, W., Jungen, M.: Universal Gaussian basis sets for an optimum representation of Rydberg and continuum wavefunctions. *J. Phys. B: Atom. Mol. Opt. Phys.* **22**(14), 2223–2240 (1989) <https://doi.org/10.1088/0953-4075/22/14/007>
- [8] Kállay, M., Nagy, P.R., Mester, D., Rolik, Z., Samu, G., Csontos, J., Csóka, J., Szabó, P.B., Gyevi-Nagy, L., Hégyely, B., Ladjánszki, I., Szegedy, L., Ladóczki, B., Petrov, K., Farkas, M., Mezei, P.D., Ganyecz, Á.: The MRCC program system: Accurate quantum chemistry from water to proteins. *J. Chem. Phys.* **152**(7), 074107 (2020) <https://doi.org/10.1063/1.5142048>
- [9] Kállay, Mihály and Nagy, Péter R. and Mester, Dávid and Gyevi-Nagy, László and Csóka, József and Szabó, P. Bernát and Rolik, Zoltán and Samu, Gyula and Csontos, József and Hégyely, Bence and Ganyecz, Ádám and Ladjánszki, István and Szegedy, Lóránt and Ladóczki, Bence and Petrov, Klára and Farkas, Máté and Mezei, Pál D. and Horváth, Réka Anna : MRCC, a quantum chemical program suite. <https://mrcc.hu/>. Accessed: 2023-11-10 (2023)

- [10] Kállay, M., Surján, P.R.: Higher excitations in coupled-cluster theory. *J. Chem. Phys.* **115**(7), 2945–2954 (2001) <https://doi.org/10.1063/1.1383290>
- [11] TURBOMOLE V7.5 2020, a development of University of Karlsruhe and Forschungszentrum Karlsruhe GmbH, 1989-2007, TURBOMOLE GmbH, since 2007; available from <https://www.turbomole.org>.
- [12] Balasubramani, S.G., Chen, G.P., Coriani, S., Diedenhofen, M., Frank, M.S., Franzke, Y.J., Furche, F., Grotjahn, R., Harding, M.E., Hättig, C., Hellweg, A., Helmich-Paris, B., Holzer, C., Huniar, U., Kaupp, M., Marefat Khah, A., Karbalaee Khani, S., Müller, T., Mack, F., Nguyen, B.D., Parker, S.M., Perlt, E., Rappoport, D., Reiter, K., Roy, S., Rückert, M., Schmitz, G., Sierka, M., Tapavicza, E., Tew, D.P., Wüllen, C., Voora, V.K., Weigend, F., Wodyński, A., Yu, J.M.: Turbomole: Modular program suite for *ab initio* quantum-chemical and condensed-matter simulations. *J. Chem. Phys.* **152**, 184107 (2020) <https://doi.org/10.1063/5.0004635>
- [13] Klamt, A., Schüürmann, G.: Cosmo: a new approach to dielectric screening in solvents with explicit expressions for the screening energy and its gradient. *J. Chem. Soc., Perkin Trans. 2*, 799–805 (1993) <https://doi.org/10.1039/P29930000799>
- [14] Karbalaee Khani, S., Marefat Khah, A., Hättig, C.: COSMO-RI-ADC(2) excitation energies and excited state gradients. *Phys. Chem. Chem. Phys.* **20**, 16354–16363 (2018) <https://doi.org/10.1039/C8CP00643A>
- [15] Xie, W., Sapunar, M., Došlić, N., Sala, M., Domcke, W.: Assessing the performance of trajectory surface hopping methods: Ultrafast internal conversion in pyrazine. *The Journal of Chemical Physics* **150**(15), 154119 (2019)
- [16] Piteša, T., Sapunar, M., Ponzi, A., Gelin, M.F., Došlić, N., Domcke, W., Decleva, P.: Combined surface-hopping, dyson orbital, and b-spline approach for the computation of time-resolved photoelectron spectroscopy signals: The internal conversion in pyrazine. *Journal of Chemical Theory and Computation* **17**(8), 5098–5109 (2021)
- [17] Sapunar, M., Piteša, T., Davidović, D., Došlić, N.: Highly Efficient Algorithms for CIS Type Excited State Wave Function Overlaps. *J. Chem. Theory Comput.* **15**(6), 3461–3469 (2019) <https://doi.org/10.1021/acs.jctc.9b00235> . Accessed 2023-03-22
- [18] Sala, M., Lasorne, B., Gatti, F., Guérin, S.: The role of the low-lying dark $n\pi^*$ states in the photophysics of pyrazine: a quantum dynamics study. *Physical Chemistry Chemical Physics* **16**(30), 15957–15967 (2014)
- [19] Beck, M.H., Jäckle, A., Worth, G.A., Meyer, H.-D.: The multiconfiguration

- time-dependent Hartree (MCTDH) method: A highly efficient algorithm for propagating wavepackets. *Phys. Rep.* **324**(1), 1–105 (2000) [https://doi.org/10.1016/S0370-1573\(99\)00047-2](https://doi.org/10.1016/S0370-1573(99)00047-2)
- [20] Meyer, H.-D., Manthe, U., Cederbaum, L.S.: The multi-configurational time-dependent Hartree approach. *Chem. Phys. Lett.* **165**(1), 73–78 (1990) [https://doi.org/10.1016/0009-2614\(90\)87014-I](https://doi.org/10.1016/0009-2614(90)87014-I)
- [21] G. A. Worth, K. Giri, G. W. Richings, I. Burghardt, M. H. Beck, A. Jäckle, and H.-D. Meyer. The QUANTICS Package, Version 1.1, (2015), University of Birmingham, Birmingham, U.K.
- [22] Yin, Z., Luu, T.T., Wörner, H.J.: Few-cycle high-harmonic generation in liquids: in-operando thickness measurement of flat microjets. *Journal of Physics: Photonics* **2**(4), 044007 (2020)
- [23] Ekimova, M., Quevedo, W., Faubel, M., Wernet, P., Nibbering, E.T.J.: A liquid flatjet system for solution phase soft-x-ray spectroscopy. *Structural Dynamics* **2**(5), 054301 (2015) <https://doi.org/10.1063/1.4928715>
- [24] Füle, M., Kovács, A., Gilinger, T., Karnok, M., Gaál, P., Figul, S., Marowsky, G., Osvay, K.: Development of an ultrathin liquid sheet target for laser ion acceleration at high repetition rates in the khz-range. *High Power Laser Science and Engineering*, 1–24
- [25] Peral, F., Gallego, E.: A study by ultraviolet spectroscopy on the self-association of diazines in aqueous solution. *Spectrochim. Acta Part A* **59**(6), 1223–1237 (2003) [https://doi.org/10.1016/S1386-1425\(02\)00304-9](https://doi.org/10.1016/S1386-1425(02)00304-9)
- [26] Feng, J.-Y., Lee, Y.-P., Hsu, P.-J., Kuo, J.-L., Ebata, T.: Structures of (Pyrazine)₂ and (Pyrazine)(Benzene) Dimers Investigated with Infrared–Vacuum Ultraviolet Spectroscopy and Quantum-Chemical Calculations: Competition among π – π , CH \cdots π , and CH \cdots N Interactions. *J. Phys. Chem. A* **127**(19), 4291–4301 (2023) <https://doi.org/10.1021/acs.jpca.3c01767> <https://arxiv.org/abs/https://doi.org/10.1021/acs.jpca.3c01767>
- [27] Tsuru, S., Sharma, B., Marx, D., Hättig, C.: Structural sampling and solvation models for the simulation of electronic spectra: Pyrazine as a case study. *Journal of Chemical Theory and Computation* **19**(8), 2291–2303 (2023) <https://doi.org/10.1021/acs.jctc.2c01129>